A&A 644, A175 (2020)
https://doi.org/10.1051/0004-6361/202039136

Astronomy & Astrophysics

SUPER

III. Broad line region properties of AGNs at $z \sim 2$

G. Vietri[1,2,3], V. Mainieri[3], D. Kakkad[3,4], H. Netzer[5], M. Perna[6,7], C. Circosta[3,8], C. M. Harrison[9], L. Zappacosta[10], B. Husemann[11], P. Padovani[3], M. Bischetti[12], A. Bongiorno[10], M. Brusa[13,14], S. Carniani[15], C. Cicone[16], A. Comastri[14], G. Cresci[7], C. Feruglio[12], F. Fiore[12], G. Lanzuisi[14], F. Mannucci[7], A. Marconi[7,17], E. Piconcelli[10], A. Puglisi[18,19,20], M. Salvato[21], M. Schramm[22], A. Schulze[23], J. Scholtz[20,24], C. Vignali[13,14], and G. Zamorani[14]

(Affiliations can be found after the references)

Received 10 August 2020 / Accepted 13 October 2020

ABSTRACT

Aims. The SINFONI survey for Unveiling the Physics and Effect of Radiative feedback (SUPER) was designed to conduct a blind search for AGN-driven outflows on X-ray-selected AGNs at redshift $z \sim 2$ with high (∼2 kpc) spatial resolution, and to correlate them with the properties of their host galaxy and central black hole. The main aims of this paper are: (a) to derive reliable estimates for the masses of the black holes and accretion rates for the Type-1 AGNs in this survey; and (b) to characterise the properties of the AGN-driven winds in the broad line region (BLR).

Methods. We analysed rest-frame optical and UV spectra of 21 Type-1 AGNs. We used Hα, Hβ, and MgII line profiles to estimate the masses of the black holes. We used the blueshift of the CIV line profile to trace the presence of winds in the BLR.

Results. We find that the Hα and Hβ line widths are strongly correlated, as is the line continuum luminosity at 5100 Å with Hα line luminosity, resulting in a well-defined correlation between black hole masses estimated from Hα and Hβ. Using these lines, we estimate that the black hole masses for our objects are in the range Log $(M_{\rm BH}/M_{\odot}) = 8.4$–$10.8$ and are accreting at $\lambda_{\rm Edd} = 0.04$–1.3. Furthermore, we confirm the well-known finding that the CIV line width does not correlate with the Balmer lines and the peak of the line profile is blueshifted with respect to the [OIII]-based systemic redshift. These findings support the idea that the CIV line is tracing outflowing gas in the BLR for which we estimated velocities up to ∼4700 km s^{-1}. We confirm the strong dependence of the BLR wind velocity on the UV-to-X-ray continuum slope, the bolometric luminosity, and Eddington ratio. We infer BLR mass outflow rates in the range 0.005–3 $M_{\odot}$ yr^{-1}, revealing a correlation with the bolometric luminosity consistent with that observed for ionised winds in the narrow line region (NLR), and X-ray winds detected in local AGNs, and kinetic power $\sim 10^{-7}$–$10^{-4} \times L_{\rm Bol}$. The coupling efficiencies predicted by AGN-feedback models are much higher than the values reported for the BLR winds in the SUPER sample; although it should be noted that only a fraction of the energy injected by the AGN into the surrounding medium is expected to become kinetic power in the outflow. Finally, we find an anti-correlation between the equivalent width of the [OIII] line and the CIV velocity shift, and a positive correlation between this latter parameter and [OIII] outflow velocity. These findings, for the first time in an unbiased sample of AGNs at $z \sim 2$, support a scenario where BLR winds are connected to galaxy-scale detected outflows, and are therefore capable of affecting the gas in the NLR located at kiloparsec scale distances.

Key words. galaxies: active – galaxies: evolution – galaxies: high-redshift – quasars: emission lines – quasars: supermassive black holes

1. Introduction

Supermassive black holes (SMBHs) are thought to be at the centre of almost all massive galaxies (Magorrian et al. 1998, Gebhardt et al. 2000). The mass of black holes ($M_{\rm BH}$) is known to be correlated with the luminosity, velocity dispersion, and stellar masses of the host-galaxy, suggesting co-evolution between the central engine and its host galaxy (Magorrian et al. 1998, Gebhardt et al. 2000, Ferrarese & Merritt 2000). A prerequisite for studying the interplay between the central AGN and its host is therefore an accurate measurement of $M_{\rm BH}$.

Direct measurement of $M_{\rm BH}$ is possible via reverberation mapping (RM), a technique that uses the lag between the variability in the AGN continuum and broad emission lines to measure the size of the broad line region (BLR).

In addition, RM experiments provide empirical relations between the radius of the BLR ($R_{\rm BLR}$) and the luminosity of the AGN, namely $R_{\rm BLR} \propto (\lambda L_{\lambda})^{\alpha}$, with $\alpha \sim 0.5$–0.7 (Kaspi et al. 2000, 2005; Bentz et al. 2009, 2013). This BLR radius–luminosity relation provides an indirect way of measuring $M_{\rm BH}$ when reverberation data are unobtainable (the so-called single epoch (SE) method; see e.g. McLure & Jarvis 2002, Shen 2013). Line luminosities, such as for example $L(\rm H_{\beta})$, can be used to replace the continuum luminosity L_{λ}.

Assuming that the BLR is virialized and the clouds are dominated by gravitational motions, the BH mass can be estimated as follows:

$$M_{\rm BH} = f \frac{R_{\rm BLR}\, V^2_{\rm BLR}}{G} \propto f \frac{(\lambda L_{\lambda})^{\alpha}\, V^2_{\rm BLR}}{G}, \quad (1)$$

where G is the gravitational constant and $v_{\rm BLR}$ is the gas velocity, which can be measured from the width of a specific emission line (full width half maximum (FWHM) or velocity dispersion, σ). The FWHM is more widely used, being less vulnerable to noise in line wings and continuum placement. The alternative velocity dispersion (σ) is less sensitive to narrow-line removal but is ill-defined for Lorentzian profiles and is sensitive to the quality of the data. In this paper we use the FWHM as indicator of the virial velocity of the gas in the BLR.

The factor f in Eq. (1) depends on the geometry and kinematics of the BLR, and can be determined by comparing $M_{\rm BH}$ derived from alternative methods (Woo et al. 2015, Graham et al. 2016). Mejía-Restrepo et al. (2018) suggested a new way to estimate f based on a strong anti-correlation between $M_{\rm BH}$ and the

FWHM of the broad emission lines, which is probably caused by line-of-sight inclination effects.

Continuum luminosity at 5100 Å is usually preferred in Eq. (1) given its tight correlation with BLR size based on a large number of sources. The line luminosities are useful in case of contamination by host starlight (Greene & Ho 2005) or in case of radio-loud objects, where the continuum is contaminated by the non-thermal emission of the jet (Wu et al. 2004).

Different lines have been used to estimate $M_{\rm BH}$ depending on redshift, such as for example Hβ, Hα, MgII, and CIV with different measurements of the line width, that is, FWHM or line dispersion (Vestergaard 2002, McLure & Jarvis 2002, Wang et al. 2009). The Hβ line width was used to measure the R–L relation in most RM studies of low-redshift AGNs (e.g. Bentz et al. 2009). As confirmed by earlier studies, there is a strong correlation among the widths of Hα, Hβ, and MgII (Greene & Ho 2005; Shen et al. 2008; McGill et al. 2008; Trakhtenbrot & Netzer 2012; Mejía-Restrepo et al. 2016). Because the majority of RM experiments used low-z AGNs, the BH mass estimates based on Balmer lines are considered the most reliable. The use of high-ionization lines such as CIV to measure $M_{\rm BH}$ is instead highly debated in the literature. It is well known that CIV usually exhibits blueshifted peak associated with gas in a non-virial motion (Gaskell 1982, Sulentic et al. 2000, Baskin & Laor 2005, Richards et al. 2011, Denney 2012, Coatman et al. 2017, Mejía-Restrepo et al. 2018, Vietri et al. 2018), which leads to a biased estimation of the BH mass. It is now well-established that the velocity shift of the CIV line peak correlates with AGN properties such as its luminosity, Eddington ratio ($\lambda_{\rm edd}$), and quasar spectral energy distribution (SED) properties (e.g. Richards et al. 2011). While these properties are a limitation in the use of CIV as an estimator of $M_{\rm BH}$, they offer the possibility to trace AGN winds on the parsec scale of the BLR.

In this paper we analyse the properties of the BLR in the SUPER sample. As described in Circosta et al. (2018), the SUPER survey consists of SINFONI observations of 39 blindly selected X-ray AGNs at a redshift of ∼2. The survey provides high-resolution, spatially resolved SINFONI observations in the H and K bands, with the main scientific goal being to infer the impact of outflows on ongoing star formation and link outflow properties with AGN and host-galaxy parameters (see Circosta et al. 2018 for further details). The objects are selected from the COSMOS-Legacy (e.g. Civano et al. 2016, Suh et al. 2015, 2020), the wide-area XMM-XXL (e.g. Georgakakis & Nandra 2011, Liu et al. 2016, Menzel et al. 2016), Stripe 82 X-ray survey (LaMassa et al. 2016), and WISSH surveys (Bischetti et al. 2017, Martocchia et al. 2017, Duras et al. 2017, Vietri et al. 2018), and about 58% are Type-1 AGNs. We focus on the 21 Type-1 AGNs observed with SINFONI (see Fig. 1) both in H and K bands, with the aim being to measure $M_{\rm BH}$ and Eddington ratio from Hβ and Hα emission lines, and to compare the results with the MgII and CIV-based measurements thanks to ancillary UV rest-frame data. Furthermore, we use the CIV line profile to trace the winds at parsec scale in order to derive the energetics of the winds and possibly link the BLR wind properties with the winds located at kiloparsec scale distances in the narrow line region (NLR). Throughout this paper we assume $H_0 = 70\,{\rm km\,s^{-1}\,Mpc^{-1}}$, $\Omega_\Lambda = 0.7$, and $\Omega_m = 0.3$, wavelengths in vacuum and line blueshifts defined as positive values.

2. Observations and data reduction

SINFONI observations were carried out as part of the ESO large programme 196.A-0377, with 3″ × 3″ field of view in adaptive optics(AO)-assisted mode, with a pixel scale of 0.05 × 0.1 arcsec (final resampled pixel scale 0.05 × 0.05 arcsec), using H grating with a resolution of R = 3000 to trace rest-frame optical region Hβ-[OIII]λ5008, and K grating with a resolution of R = 4000 to trace lines from Hα up to [SII]λ6716,6731. We acquired six observation frames with exposure times of 600 s for each observing block using the pattern "O–O–O–O–O–O" (O = object) as observation strategy for a good sky subtraction; in case of extended sources dedicated sky exposures were acquired (O–S–O–O–S–O). The total on-source exposure time ranges from 1 hr up to 6 hr. We refer to Kakkad et al. (2020) for a detailed description of the SINFONI data reduction, but below we report the main steps. We used the ESO pipeline (3.1.1) which returns science, PSF, and distortion-corrected and wavelength-calibrated telluric cubes. The background sky emission was removed with the IDL routine SKYSUB (Davies 2007). We corrected the telluric absorption in the science frames by removing the telluric lines from the observed telluric standard star, which was observed close in time and airmass to the object. The response curve was determined by normalising the telluric-free star spectrum divided by a blackbody spectrum and then applied to the science and standard star cubes. The spectrum extracted from the telluric-free star cube was then convolved with a 2MASS transmission filter, H or K according to the SINFONI observation bands, to derive the conversion factor from count to appropriate physical unit, which was then applied to the science cube. The flux-calibrated frames were then combined using a dedicated SINFONI pipeline recipe. For observations taken during the same night, we stacked the individual observing blocks according to the centre position of the image recorded in the header. For observations carried out on different nights, we first determined the relative offset of the centroids of the images, performing a two-dimensional Gaussian fit, and then re-aligned and co-added the individual observing blocks. Twenty-one Type-1 AGNs were observed both in the H and K bands. However, one target was not detected in continuum or in emission lines in the H band but was detected in the K band, namely X_N_53_3, and one lacks emission lines in the H band but was detected in continuum and in lines in the K band, namely X_N_44_64.

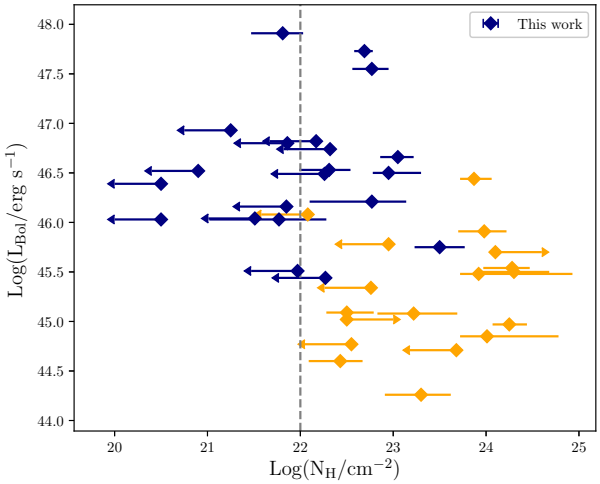

Fig. 1. Bolometric luminosity vs. column density of the SUPER sample of AGNs. The dashed line at $\log(N_{\rm H}\,{\rm cm^2}) = 22$ marks the assumed separation between X-ray unobscured and obscured AGN. The Type-1 SUPER targets analysed in the present paper are represented as blue diamonds.

3. Spectroscopic analysis

We extracted the integrated spectra from a circular region centred at the QSO position, which covers at least 95% of the total

Table 1. Properties of the SUPER AGNs considered in this paper.

ID (1)	RA (2)	Dec (3)	z (4)	$z_{[OIII]}$ (5)	H (6)	K (7)	r_H (8)	r_K (9)	Log (L_{Bol}/erg s^{-1}) (10)	Log (L_{5100}/erg s^{-1}) (11)
X_N_160_22	02:04:53.81	−06:04:07.82	2.445	2.442	19.22	18.79	0.5	0.4	46.74 ± 0.02	45.83 ± 0.06
X_N_81_44	02:17:30.95	−04:18:23.66	2.311	2.317	18.78	18.43	0.45	0.4	46.80 ± 0.03	45.75 ± 0.06
X_N_53_3	02:20:29.84	−02:56:23.41	2.434	2.433	20.60	–	–	0.2	46.21 ± 0.03	–
X_N_66_23	02:22:33.64	−05:49:02.73	2.386	2.385	20.56	20.33	0.35	0.45	46.04 ± 0.02	45.63 ± 0.06
X_N_35_20	02:24:02.71	05:11:30.82	2.261	2.261	22.07	21.70	0.15	0.2	45.44 ± 0.02	43.95 ± 0.06
X_N_12_26	02:25:50.09	−03:06:41.16	2.471	2.472	19.83	19.53	0.4	0.35	46.52 ± 0.02	45.53 ± 0.06
X_N_44_64	02:27:01.46	−04:05:06.73	2.252	2.244	21.31	20.77	–	0.2	45.51 ± 0.07	–
X_N_4_48	02:27:44.63	−03:42:05.46	2.317	2.315	19.57	20.43	0.25	0.35	46.16 ± 0.02	45.05 ± 0.06
X_N_102_35	02:29:05.94	04:02:42.99	2.190	2.190	18.76	18.19	0.15	0.15	46.82 ± 0.02	45.52 ± 0.06
X_N_115_23	02:30:05.66	−05:08:14.10	2.342	2.340	19.79	19.26	0.35	0.4	46.49 ± 0.02	45.55 ± 0.06
cid_166	09:58:58.68	+02:01:39.22	2.448	2.461	18.55	18.23	0.3	0.45	46.93 ± 0.02	45.83 ± 0.06
cid_1605	09:59:19.82	+02:42:38.73	2.121	2.118	20.63	20.14	0.2	0.2	46.03 ± 0.02	44.84 ± 0.06
cid_346	09:59:43.41	+02:07:07.44	2.194	2.217	19.24	18.95	0.35	0.40	46.66 ± 0.02	45.61 ± 0.06
cid_1205	10:00:02.57	+02:19:58.68	2.255	2.257	21.64	20.72	0.15	0.6	45.75 ± 0.17	44.91 ± 0.06
cid_467	10:00:24.48	+02:06:19.76	2.288	2.285	19.34	18.91	0.2	0.2	46.53 ± 0.04	45.25 ± 0.06
J1333+1649	13:33:35.79	16:49:03.96	2.089	2.099	15.72	15.49	0.55	0.5	47.91 ± 0.02	47.32 ± 0.06
J1441+0454	14:41:05.54	+04:54:54.96	2.059	2.080	17.15	16.53	0.50	0.55	47.55 ± 0.02	46.66 ± 0.06
J1549+1245	15:49:38.73	+12:45:09.20	2.365	2.368	15.92	15.34	0.50	0.65	47.73 ± 0.04	47.16 ± 0.06
S82X1905	23:28:56.35	−00:30:11.74	2.263	2.273	19.72	19.15	0.4	0.35	46.50 ± 0.02	45.55 ± 0.06
S82X1940	23:29:40.28	−00:17:51.68	2.351	2.350	20.80	20.15	0.3	0.3	46.03 ± 0.02	44.98 ± 0.06
S82X2058	23:31:58.62	−00:54:10.44	2.308	2.315	19.79	19.29	0.3	0.35	46.39 ± 0.02	45.54 ± 0.06

Notes. Columns give the following information: (1) target identification, (2–3) celestial coordinates, (4) redshift from archival optical spectra, (5) redshift from the peak location of the [OIII]λ5008 in the integrated spectra, (6–7) 2MASS photometric data, (8–9) the radius (in arcsec) of the circular aperture centred on the target used to extract the spectrum for the H and K bands, (10) logarithm of the bolometric luminosity derived from SED fitting (Circosta et al. 2018), and (11) logarithm of the extinction-corrected luminosity at 5100 Å derived from the best-fit values of the power-law model representing the AGN continuum (see Sect. 3).

emission. The target centre was found using a 2D Gaussian fit on the wavelength-collapsed image from the datacube over the entire wavelength range of the SINFONI observations. The radius of the extraction region is on average ∼0.3 (∼0.4) arcsec, with a minimum value of 0.15 (0.15) arcsec and a maximum value of 0.55 (0.65) arcsec for H (K) band (see Table 1). In the following, we provide a detailed description of our analysis of the line profile for the Hβ-[OIII]λ5008 complex extracted from the H band datacube, and the Hα-[NII]-[SII] region extracted from the K band data.

3.1. Modelling SINFONI spectra

We performed the fit for the H and K band spectra separately using the python routine `scipy.optimize.curve_fit`. The sky line residuals were masked from the spectrum during the fitting procedure. We shifted the H and K band spectra to the rest frame using the spectroscopic redshift obtained from the peak location of the [OIII]λ5008 (hereafter [OIII]) in the integrated spectrum[1].

H band. We modelled the spectra using a simultaneous fit of the continuum, the [OIII] doublet, the Hβ emission line, and the iron emission lines. A power law was adopted to model the continuum, while Gaussian components were used to reproduce the emission lines. Specifically, we used (i) up to two Gaussian components to model the emission from the NLR of the [OIII] doublet and Hβ emission lines, and the addition of the second Gaussian depended on whether or not it minimises the reduced chi-square value of the overall model; and (ii) a Gaussian component or broken power-law for fitting the Hβ emission from the BLR. For the NLR components of [OIII] and Hβ, we fixed the wavelength separation and assumed equal broadening for the lines assuming the same gas is responsible for the those emission lines. The flux ratio for the components of the [OIII] doublet was set to 1:3, according to their atomic parameters.

The iron emission is modelled with three observational templates, namely those of Boroson & Green (1992), Véron-Cetty et al. (2004), and Tsuzuki et al. (2006). These empirical templates are anchored to the [OIII] rest frame and each iron template is convolved with a single Gaussian component with FWHM in the range 1000–5000 km s^{-1}. A χ^2 minimisation procedure was used to select the best-fit FeII template[2].

Finally, we also modelled the HeIIλ4686 line with two components: (1) a narrow Gaussian with centroid and velocity dispersion tied to the narrow [OIII] line; and (2) a broad Gaussian component with parameters free to vary to reproduce the emission due to the BLR. Only in one case, X_N_160_22, we did unambiguously detect the HeII narrow component with $FWHM = 920 \pm 50$ km s^{-1}. We do not detect the HeII BLR component, this is probably due to the difficult deblending of this component from the underlying iron emission. Figure 2 shows an example of the H band fit (see Appendix A for the rest of the

[1] For the two sources undetected in the H-band (X_N_53_3 and X_N_44_64), we used the redshift obtained from the Hα narrow component.

[2] To test the effect of the three FeII templates on the FWHM measurements, we fitted one spectrum, X_N_81_44, with all three templates and the BH masses are consistent within the uncertainties, namely Log($M_{BH}/M_\odot$) = 8.77 ± 0.30, Log($M_{BH}/M_\odot$) = 9.05 ± 0.30 and Log($M_{BH}/M_\odot$) = 8.81 ± 0.30, for Véron-Cetty et al. (2004), Boroson & Green (1992) and Tsuzuki et al. (2006), respectively.

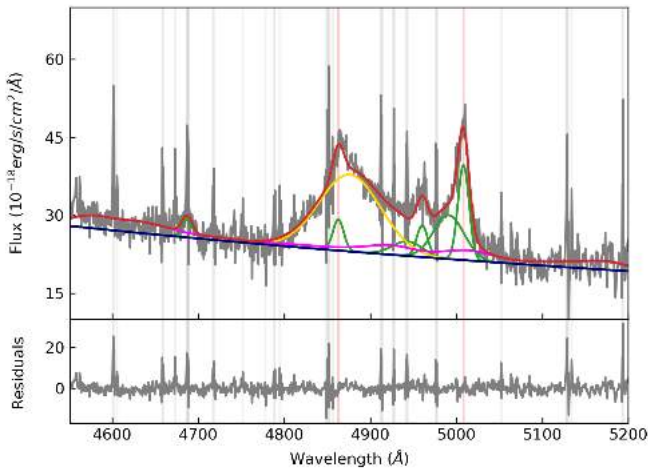

Fig. 2. Parametrisation of the Hβ-[OIII] region of the SUPER AGN X_N_160_22. The red curve shows the best fit to the data. Green Gaussian lines refer to the Gaussian components used to reproduce the line profile of each emission line. The gold Gaussian component indicates the broad component of Hβ associated with BLR emission. FeII emission is marked in magenta. The *lower panel* shows the fit residuals. Grey bands indicate the sky line residuals masked during the fit procedure. The *x*- and *y*-axes show the rest-frame wavelength and flux (not corrected for extinction) according to the redshift of the target, respectively.

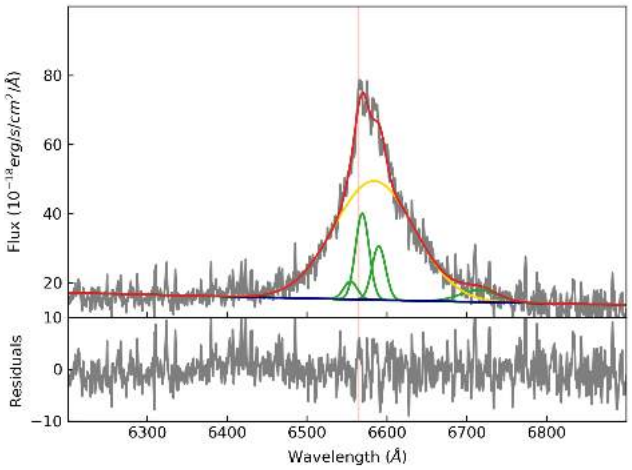

Fig. 3. Parametrisation of the Hα region of the SUPER AGN X_N_160_22. The red curve shows the best fit to the data. Green Gaussian lines refer to the narrow and broad components used to reproduce the line profile of Hα, [NII], and [SII]. The gold Gaussian component indicates the broad component of Hα associated with BLR emission. The *lower panel* shows the fit residuals. The *x*- and *y*-axes show the rest-frame wavelength and flux (not corrected for extinction), according to the redshift of the target, respectively.

Table 2. Properties of BLR components of the Hβ emission line derived from parametric model fits.

ID	$\lambda^{\rm BLR}_{\rm H\beta}$ (Å)	$FWHM^{\rm BLR}_{\rm H\beta}$ (km s^{-1})	$EW^{\rm BLR}_{\rm H\beta}$ (Å)	Log ($L^{\rm BLR}_{\rm H\beta}$/erg s^{-1})
X_N_160_22	4876 ± 1	5190 ± 170	58 ± 2	43.99 ± 0.04
X_N_81_44	4873 ± 1	5290 ± 170	57 ± 2	43.87 ± 0.04
X_N_12_26	4865 ± 1	4890 ± 200	51 ± 2	43.58 ± 0.04
X_N_4_48	4860 ± 4	6710 ± 670	40 ± 4	42.95 ± 0.06
X_N_102_35	4872 ± 1	4810 ± 160	58 ± 2	43.67 ± 0.04
X_N_115_23	4869 ± 2	6330 ± 250	56 ± 2	43.68 ± 0.04
cid_166	4867 ± 1	6970 ± 130	91 ± 2	44.17 ± 0.04
cid_1605	4860 ± 3	5040 ± 510	156 ± 22	43.25 ± 0.06
cid_346	4870 ± 2	6280 ± 340	46 ± 2	43.63 ± 0.05
cid_467	4875 ± 5	9260 ± 760	93 ± 8	43.62 ± 0.05
J1333+1649	4841 ± 7	6300 ± 250	42 ± 2	45.34 ± 0.04
J1441+0454	4855 ± 1	4030 ± 100	47 ± 1	44.73 ± 0.04
J1549+1245	4867 ± 2	16570 ± 690	108 ± 7	45.53 ± 0.05
S82X1905	4872 ± 1	4960 ± 100	71 ± 1	43.80 ± 0.04
S82X1940	4862 ± 1	3710 ± 140	75 ± 3	43.24 ± 0.04
S82X2058	4860 ± 1	6450 ± 150	69 ± 1	43.78 ± 0.04

Notes. Columns give the following information for the BLR component of the Hβ emission line: (1) target identification, (2) centroid (Å), (3) FWHM (km s^{-1}), (4) rest-frame EW (Å), (5) logarithm of the extinction-corrected Hβ luminosity.

sample). Table 2 provides the best-fit parameter of the Hβ BLR emission lines component for the 16/21[3] SUPER targets with Hβ BLR detection.

K band. We modelled the continuum by adopting a power-law function and emission lines by using the same modelling as for the [OIII] emission profile, for the Hα, [NII], and [SII] doublet emission lines. In cases where we used one Gaussian component to reproduce the [OIII] profile, we used one Gaussian model to reproduce the NLR emission of the *K* band lines and tied together the centroid and velocity dispersion of the *K* band lines, allowing the centroid to vary in the range of 7 Å and the velocity dispersion to vary up to the values derived for the [OIII] one-Gaussian component. In case of two Gaussians for the [OIII] profile, we used two Gaussian components for the NLR emission of the *K* band, and for the second Gaussian the same broadening of the second [OIII] Gaussian component was adopted with a fixed wavelength separation between the [OIII] and *K* band lines centroid.

We also fitted a BLR Gaussian component for the Hα line. This parametrisation reduced the possibility of model degeneracy. We note that for cid_346 we also use a narrow component to reproduce the Hα-region profile which was clearly detected in the spectrum ([OIII] profile was modelled with one Gaussian component).

The flux intensities of the [NII] doublet were set to 1:3 according to their atomic parameters. Figure 3 shows an example of the *K* band fit (see Appendix A for the rest of the sample). Table 3 provides the best-fit parameter of the Hα BLR emission line components for all the SUPER targets.

3.2. Modelling the UV spectra

We retrieved the rest-frame UV spectra for our targets from the SDSS archive for all but cid_1205, for which we used the archival VIMOS/VLT spectrum. We did not analyse the spectrum of X_N_44_64 because of the very low S/N. The observed UV wavelengths were shifted to the systemic redshift (see Sect. 3). The presence of strong iron features and Balmer continuum emission in the MgIIλ2800 Å region make the continuum level difficult to estimate. We therefore fit the wavelength region from Lyα up to CIII]λ1909 Å (less affected by the iron emission) and the MgII-FeII region (2600–3000 Å) separately.

[3] The *H* band datacube of cid_1205 is contaminated by a bright stripe at the location of Hβ line preventing reliable measurement of the line parameters. We therefore did not estimate BLR Hβ line parameters for this source.

Table 3. Properties of BLR components of the Hα emission line derived from parametric model fits.

ID	$\lambda^{\rm BLR}_{\rm H\alpha}$ (Å)	$FWHM^{\rm BLR}_{\rm H\alpha}$ (km s^{-1})	$EW^{\rm BLR}_{\rm H\alpha}$ (Å)	Log ($L^{\rm BLR}_{\rm H\alpha}$/erg s^{-1})
X_N_160_22	6584 ± 1	5410 ± 110	289 ± 7	44.46 ± 0.03
X_N_81_44	6580 ± 1	6320 ± 120	267 ± 5	44.41 ± 0.03
X_N_53_3	6571 ± 1	4630 ± 180	415 ± 27	43.57 ± 0.03
X_N_66_23	6567 ± 2	6105 ± 310	254 ± 15	43.86 ± 0.03
X_N_35_20	6564 ± 7	6440 ± 1590	317 ± 92	42.80 ± 0.08
X_N_12_26	6570 ± 1	5270 ± 120	256 ± 7	44.03 ± 0.03
X_N_44_64	6567 ± 5	7720 ± 720	187 ± 21	43.15 ± 0.04
X_N_4_48	6573 ± 2	7700 ± 240	377 ± 19	44.27 ± 0.03
X_N_102_35	6577 ± 1	5190 ± 100	292 ± 7	44.16 ± 0.03
X_N_115_23	6572 ± 1	6560 ± 130	335 ± 8	44.28 ± 0.03
cid_166	6570 ± 1	6810 ± 100	437 ± 8	44.76 ± 0.03
cid_1605	6569 ± 2	3690 ± 230	296 ± 20	43.55 ± 0.04
cid_346	6565 ± 2	6980 ± 260	205 ± 9	44.12 ± 0.03
cid_1205	6564 ± 2	5100 ± 230	542 ± 42	43.52 ± 0.03
cid_467	6569 ± 2	8450 ± 230	458 ± 21	44.11 ± 0.03
J1333+1649	6572 ± 1	6190 ± 50	217 ± 2	45.73 ± 0.03
J1441+0454	6559 ± 1	4740 ± 30	169 ± 2	45.09 ± 0.03
J1549+1245	6580 ± 1	7270 ± 50	304 ± 2	45.80 ± 0.03
S82X1905	6571 ± 1	4730 ± 50	360 ± 6	44.17 ± 0.03
S82X1940	6563 ± 1	4370 ± 160	344 ± 16	44.35 ± 0.03
S82X2058	6558 ± 1	6400 ± 110	322 ± 6	44.17 ± 0.03

Notes. Columns give the following information for the BLR component of the Hα emission line: (1) target identification, (2) centroid (Å), (3) full width at half maximum (km s^{-1}), (4) rest-frame EW (Å), (5) logarithm of the extinction-corrected Hα luminosity.

Lyα-CIII] region. We fitted the continuum in line-free wavelength regions 1445–1455 Å and 1973–1983 Å using a power-law function. The UV lines Lyα1216, NVλ1240, Si IIλ1263, SiVλ1398 OIVλ1402, NIVλ1486, CIVλ1549, HeIIλ1640, OIII]λ1663, Al IIλ1671, Al IIIλ1857, Si IIλ1887, and CIII]λ1909 were fitted simultaneously using one Gaussian component allowing a shift of the centroid of ±10 Å and FWHM up to 10 000 km s^{-1} (e.g. Matsuoka et al. 2011, Mejía-Restrepo et al. 2016); for the CIV line, a shift of ±50 Å was used, which is justified by the usually asymmetric and shifted profile. These lines (except for the CIV line) are not necessary for the purpose of this work except for limiting the continuum placement and would require more accurate modelling to derive line parameters.

Apart from the BAL AGN cid_346 and J1549+1245 (Bruni et al. 2019), the CIV line of which is heavily affected by absorption, and for which we only used one Gaussian component to reproduce the CIV line, we performed the line fitting using both a model with a single Gaussian component and one with two Gaussians. The models were compared using the Bayesian information criterion (BIC; see Schwarz 1978), defined as BIC = χ^2 + k ln (N), where N is the number of data points and k is the number of free parameters. A BIC difference larger than 10 was the adopted criteria to choose the model with two components. For five of our targets (X_N_35_20, X_N_81_44, cid_1605, S82X1905, S82X1940) the CIV profile is better reproduced with one Gaussian component. The remaining sources are better reproduced by a two-Gaussian model fit.

The model fitting is performed in the spectral range of 1210 Å–2000 Å. We excluded from the fit the heavy blended spectral regions of OI+SII λ 1305, CIIλ1335, the so-called 1600 Å bump, the undefined feature in 1570–1631 Å (see Nagao et al. (2006) for a detailed discussion), and NIVλ1719, AlII λ1722, NIII]λ1750, and FeII multiplets, namely 1286–1357 Å, 1570–1631 Å, and 1687–1833 Å. The measured FWHM$_{\rm CIV}$ of the total profile are in the range ∼1300–10 000 km s^{-1} and the velocity shifts, defined as $v_{50}^{\rm CIV} = c \times (\lambda_{\rm half} - 1549.48)/1549.48$, with $\lambda_{\rm half}$ being the wavelength that bisects the cumulative total line flux and c the speed of light, are in the range $v_{50}^{\rm CIV} \sim -760$ up to 4700 km s^{-1}. Detailed results from the best-fit model of the CIV emission line for 20 of the 21 SUPER targets are reported in Table 4. We note that for the bulk of the SUPER sources, the total CIV profile is blueshifted and therefore it is dominated by gas not at systemic velocity but in an outflowing phase. An example of the fit is shown in the upper panel of Fig. 4 (see Appendix A for the rest of the sample).

MgIIλ2800. For 17 of the 21 SUPER sources we were able to model the MgII line, but the remaining sources have very low S/N on this line and are affected by strong sky-line residuals. We first modelled the continuum[4] with a power law plus the UV FeII+FeII templates from Popović et al. (2019) convolved with a Gaussian function with a FWHM in the range 1000–5000 km s^{-1}. The best-fit template was chosen through a χ^2 minimisation procedure. A potential velocity shift of the FeII emission lines is not considered in this paper. The MgII line was then generally modelled with a single Gaussian. For three objects whose spectra were not affected by strong sky residuals we performed the line fit using two Gaussian components. We used the BIC criterion to compare the models, and the single Gaussian model fit was favoured in all cases. We derived FWHM$_{\rm MgII}$ in the range ∼3000–9000 km s^{-1} and a velocity shift $v_{50}^{\rm MgII}$ ∼ up to 1200 km s^{-1}. We note that the MgII emission line and FeII emission surrounding the MgII are affected by sky-line residuals in almost all spectra of the SUPER sample, which can affect the measured line properties. Therefore, hereafter the MgII line properties are used with caution.

The result of the emission line fit for the MgII emission line of 17 of the 21 SUPER targets is reported in Table 5 and an example of the fit in the bottom panel of Fig. 4 (for the rest of the sample see Appendix A).

To estimate the uncertainties on the derived parameters for each of the emission lines discussed above and in Sect. 3.1 we created 1000 realisations of each spectrum by adding noise drawn from a Gaussian distribution with dispersion equal to the rms of the spectrum to the best-fit model spectrum and repeated the line-fitting procedure on these mock spectra. The associated errors are estimated using the 84th and 16th percentiles of the parameter distribution.

4. Broad line region properties

4.1. Comparison of the broad line profiles

As described in Sect. 3, the line-fitting procedure provided luminosities, emission-line centroids, and widths for four broad lines in our AGN sample (Hα, Hβ, CIV and MgII) which we now compare to derive reliable estimates of the BH masses. First we compare the best-fit values of the FWHM of the Balmer lines (Fig. 5). The FWHM of Hα and Hβ for our sample are very similar (slope = 1.43 ± 0.49), consistent with the 1:1 relation. The only exception is the source J1549+1245, for which the Hβ line

[4] We note that no Balmer continuum model is included. This results in an overestimation of the continuum level.

Table 4. Properties of the CIVλ1549 emission line derived from parametric model fits (see Sect. 3.2).

ID	$\lambda_{50}^{\rm CIV}$ (Å)	$FWHM_{\rm CIV}$ (km s^{-1})	$EW_{\rm CIV}$ (Å)	$v_{50}^{\rm CIV}$ (km s^{-1})	Log ($L_{\rm CIV}$/erg s^{-1})	Log (L_{1350}/erg s^{-1})
X_N_160_22	1548 ± 1	3180 ± 280	38 ± 1	250 ± 70	45.03 ± 0.09	46.71 ± 0.10
X_N_81_44	1546 ± 1	6790 ± 250	49 ± 2	700 ± 110	44.77 ± 0.09	46.27 ± 0.10
X_N_53_3	1547 ± 1	4910 ± 480	60 ± 2	470 ± 140	44.67 ± 0.09	46.09 ± 0.10
X_N_66_23	1548 ± 1	2350 ± 210	63 ± 2	240 ± 30	44.35 ± 0.09	45.80 ± 0.10
X_N_35_20	1545 ± 3	5550 ± 1240	33 ± 7	950 ± 520	43.56 ± 0.13	45.32 ± 0.10
X_N_12_26	1545 ± 1	3860 ± 520	30 ± 1	920 ± 140	44.49 ± 0.09	46.27 ± 0.10
X_N_4_48	1549 ± 1	5250 ± 620	34 ± 2	50 ± 140	44.41 ± 0.09	46.13 ± 0.10
X_N_102_35	1548 ± 1	3250 ± 100	53 ± 1	190 ± 70	45.14 ± 0.09	46.68 ± 0.10
X_N_115_23	1549 ± 1	2280 ± 220	61 ± 2	140 ± 70	44.79 ± 0.09	46.34 ± 0.10
cid_166	1545 ± 1	3940 ± 173	50 ± 1	850 ± 70	45.24 ± 0.09	46.79 ± 0.10
cid_1605	1550 ± 1	6090 ± 300	70 ± 3	−120 ± 130	44.30 ± 0.09	45.76 ± 0.10
cid_346	1538 ± 1	7470 ± 190	30 ± 1	2230 ± 80	44.66 ± 0.09	46.49 ± 0.10
cid_1205	1551 ± 1	1340 ± 140	60 ± 6	250 ± 60	42.34 ± 0.10	43.72 ± 0.11
cid_467	1548 ± 1	3450 ± 310	60 ± 2	280 ± 70	44.91 ± 0.09	46.51 ± 0.10
J1333+1649	1538 ± 1	5250 ± 170	19 ± 1	2300 ± 30	45.65 ± 0.09	47.61 ± 0.10
J1441+0454	1525 ± 1	9690 ± 200	24 ± 1	4690 ± 30	45.47 ± 0.09	47.33 ± 0.10
J1549+1245	1553 ± 1	5180 ± 120	18 ± 1	−760 ± 50	45.10 ± 0.09	47.01 ± 0.10
S82X1905	1544 ± 1	7250 ± 230	45 ± 1	1070 ± 100	44.63 ± 0.09	46.24 ± 0.10
S82X1940	1547 ± 1	6690 ± 260	80 ± 3	430 ± 110	44.41 ± 0.09	45.83 ± 0.10
S82X2058	1546 ± 1	4080 ± 280	28 ± 1	740 ± 140	44.61 ± 0.09	46.44 ± 0.10

Notes. Columns give the following information for the BLR component of the CIV emission line: (1) target identification, (2) centroid (Å), (3) FWHM (km s^{-1}), (4) rest-frame EW (Å), (5) velocity of the CIV at 50% of the cumulative line flux, (6) logarithm of the extinction-corrected CIV luminosity, and (7) logarithm of the extinction-corrected luminosity at 1350 Å derived from the best-fit values of the power-law model representing the AGN continuum (see Sect. 3).

shows a much broader FWHM with respect to the Hα line. We also performed a fit excluding this outlier, which resulted in a slope of 0.95 ± 0.20.

The good agreement between the FWHM of the Balmer lines is consistent with several previous results. In particular those of Greene & Ho (2005), who analysed a sample of 229 AGNs at $z \sim 0.3$ and Log (L_{5100}/erg s^{-1}) ~ 42–45 and found a strong correlation (red-dashed line in Fig. 5). More recently, Mejía-Restrepo et al. (2016) also found a correlation consistent with the 1:1 relation for a sample of 39 Type-1 AGNs at $z \sim 1.55$ with $L_{5100} > 10^{44.3}$ erg s^{-1}. This latest work has the further advantage that both lines were observed simultaneously thanks to the wide wavelength coverage of the X-shooter instrument at the VLT, thereby avoiding any issue related to the time variability of the line profile. The 1:1 correlation between the width of the Balmer lines suggests common kinematics for the Hβ and Hα lines, and hence the same emission line region, which is consistent with the similar time lags measured for these lines in reverberation mapping experiments performed to derive the size of the BLR (e.g. Kaspi et al. 2000).

We now compare the FWHM of the MgII with those of the Balmer lines. In this case, excluding the outlier X_N_4_48, which shows a very broad FWHM of the MgII, we find a significant positive correlation between the MgII and Hα and Hβ measurements, respectively (Fig. 6), consistent with several previous studies (e.g. Shen & Liu 2012; Mejía-Restrepo et al. 2016). As indicated by the slope values reported in Table 6, the MgII line is systematically narrower than the corresponding Hα. We find that on average the MgII lines are narrower than the Hβ lines, which is consistent with the 30% value reported by Mejía-Restrepo et al. (2016). The most likely explanation for this difference in line width is that MgII is emitted from a region in the BLR further out from the central SMBH than the regions emitting Hα and Hβ. Finally, one of our objects, X_N_4_48, shows FWHM(MgII) > FWHM(Hα,Hβ) (albeit affected by large uncertainties) which may not be surprising given the size of our sample: Marziani et al. (2013) reported that such an extreme population, which they named broad-MgII, represents ≈10% of bright quasars.

A completely different outcome is found for the comparison of the FWHM of the CIV with that of the previous emission lines: Hβ, Hα, and MgII FWHMs show very poor correlation with that of CIV (see Fig. 7 and Table 6). Reverberation mapping experiments, also performed on high-redshift quasars (Lira et al. 2018), predict that the emission line region of CIV is located closer to the central SMBH than that producing the Balmer lines, and therefore we would expect that FWHM(CIV) > FWHM(Balmer lines). Ten of the sixteen SUPER targets, with both Hβ and CIV lines, shows the opposite behaviour, i.e. FWHM(CIV) < FWHM(Hβ) and 13 of the 20 sources, with both Hα and CIV lines, have FWHM(CIV) < FWHM(Hα). This confirms earlier works based on larger samples of AGNs (e.g. Trakhtenbrot & Netzer (2012)) that suggested that the CIV line is an unreliable probe of the virialized gas in the BLR. In particular, Mejía-Restrepo et al. (2018) provide a systematic analysis of this behaviour, including a critical analysis of various "correction factors" suggested to mitigate this issue in the past. They concluded that this is a real effect that is probably related to non-virialized gas motion in the BLR. In addition, the FWHM of the CIV correlates with the velocity shift of the CIV emission line (Gaskell 1982, Sulentic et al. 2000, Richards et al. 2011, Denney 2012, Coatman et al. 2017, Vietri et al. 2018), leading to a further dispersion in the plane of FWHM Hβ-Hα versus CIV. Based on the above, we do not use

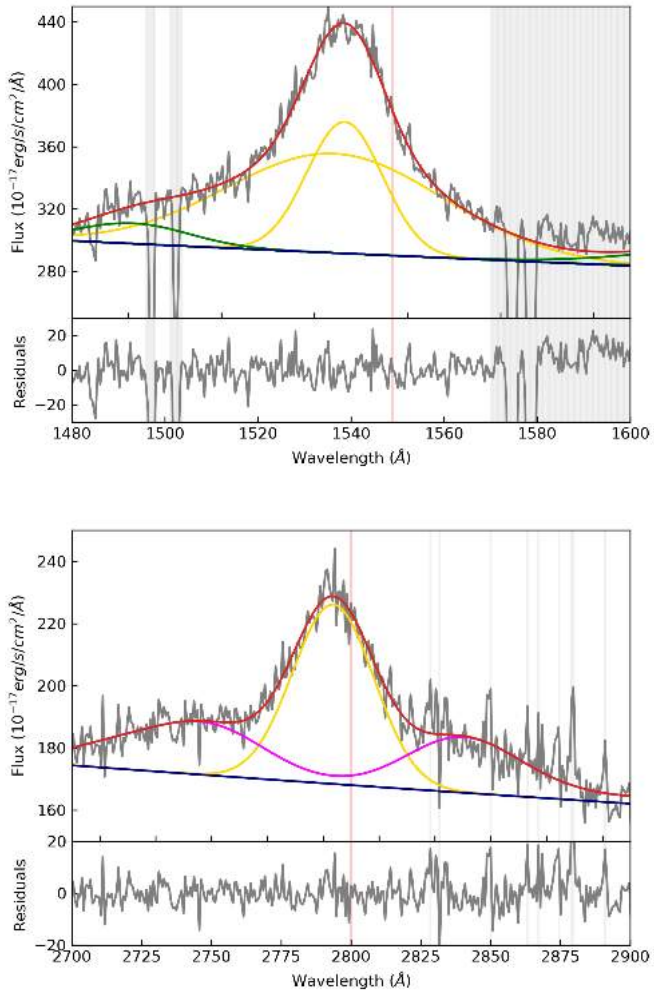

Fig. 4. *Upper*: parametrisation of the CIV emission line of the SUPER AGN J1333+1649. The red curve shows the best fit to the data and the gold curves indicate the multiple Gaussian model used to reproduce the CIV line profile. The red line indicates the expected wavelength of the CIVλ1549 based on [OIII] systemic redshift. *Bottom*: parametrisation of the MgII emission line. The red curve shows the best fit to the data and the gold curve the Gaussian component used to reproduce the MgII line profile. The magenta curve represents the best-fit model of the UV FeII emission. The red line indicates the expected wavelength of the MgIIλ2800 based on [OIII] systemic redshift. Grey bands represent the absorption and sky-line features masked during the fitting procedure.The x- and y-axes show the rest-frame wavelength and flux (not corrected for extinction) according to the redshift of the target.

CIV as a reliable BH mass estimator, but we take advantage of the ability to trace non-virialized gas at the scale of the BLR in Sect. 5.

4.2. Comparison of continuum and line luminosity

In order to correct the BLR line luminosity for dust extinction we use the ratio of the broad Balmer lines. For a low-density environment such as the NLR, the intrinsic Balmer ratio is equal to 2.74–2.86 assuming a case B recombination (Osterbrock & Ferland 2006). The BLR densities are significantly higher, and line optical depths and collisional effects can lead to different Balmer decrements (Netzer 2013). While studies of large samples of AGNs suggests that this is generally the case, the mean $L_{H\alpha}/L_{H\beta}$ of the sources with the bluest continua are surprisingly similar to the Case B prediction with values ≈3 (Baron et al. 2016). We also find a similar ratio, with a median value of 3.37 ± 0.09.

The relationship between the Balmer decrement and the colour excess is given by:

$$E(B-V) = \frac{E(H\beta - H\alpha)}{k(\lambda_{H\beta}) - k(\lambda_{H\alpha})} = \frac{2.5}{k(\lambda_{H\beta}) - k(\lambda_{H\alpha})} \log\left[\frac{(H_\alpha/H_\beta)_{obs}}{(H_\alpha/H_\beta)_{int}}\right], \quad (2)$$

where $k(\lambda_{H\beta})$ and $k(\lambda_{H\alpha})$ are the reddening curves evaluated at Hβ and Hα wavelengths respectively, and the $(H_\alpha/H_\beta)_{obs}$ and $(H_\alpha/H_\beta)_{int}$ are the observed and intrinsic Balmer decrement respectively. Based on the observed Balmer decrement, we derived the colour excess $E(B-V)$ assuming a foreground screen, a Cardelli et al. (1989) extinction law, and $(H_\alpha/H_\beta)_{int} = 3$ (Baron et al. 2016). We derived a median $E(B-V)$ of 0.12 mag with a standard deviation of 0.03 mag. We use this median value of $E(B-V)$ to correct the emission lines and continuum luminosities. This means that the luminosities are corrected by a factor of ∼1.3, ∼1.5, ∼1.9, and ∼2.4 for the emission lines Hα, Hβ, MgII, and CIV, respectively, and ∼1.4, ∼1.9, and ∼2.7 for the continuum at 5100 Å, 3000 Å, and 1350 Å, respectively. We note that reliable estimates of BH mass for the SUPER sample are based on Hα and Hβ lines (see Sect. 4.3), for which the reddening correction has a minor effect on the line luminosity.

We estimated the monochromatic luminosity at 5100 Å using the best-fit values of the power-law model representing the AGN continuum, L_{5100}. The contamination from the host-galaxy for the SUPER targets is negligible as $L_{5100} > 10^{45.4}$ erg s^{-1} (Shen et al. 2011). The values derived from the fit are consistent with the continuum luminosities at 5100 Å obtained from the SED fitting presented in Circosta et al. (2018).

In Fig. 8 we show the comparison between the extinction-corrected luminosities at 5100 Å (L_{5100}) as estimated from the best-fit continuum power-law model and the broad Hα ($L_{H\alpha}$). We find a tight correlation between the luminosities (see also Table 6), which is important for the use of Hα measurements to estimate the BH mass (see Sect. 4.3).

We also compared the extinction-corrected continuum luminosities at 5100 Å (L_{5100}), 3000 Å (L_{3000}), and 1350 Å (L_{1350}), standard continuum luminosity indicators that were used in earlier works. Both continuum luminosity at 1350 Å and 3000 Å are correlated with L_{5100}, with slopes close to unity. We list the slope, Spearman coefficient, and p-value of the correlations discussed in Table 6. The results from our small SUPER sample are similar but not identical to those found in larger samples by Shen & Liu (2012) and Mejía-Restrepo et al. (2016). Again, we note that unlike the Mejia-Restrepo results, our observations are not simultaneous and variability may be a cause of the different slope and scatter.

Finally, we use extinction-corrected L_{5100} to derive the bolometric luminosity assuming a bolometric correction factor, $f_{bol} = L_{Bol}/\lambda L_\lambda$ where L_λ is the monochromatic luminosity. We used the prescription from Runnoe et al. (2012):

$$\mathrm{Log}(L_{Bol}) = 4.891 + 0.912 \times \mathrm{Log}(5100\ L_{5100}). \quad (3)$$

The bolometric luminosities obtained from Eq. (3) are consistent with those derived from the SED fitting Circosta et al. (2018). We use these latter luminosity values as our fiducial values in the rest of the paper.

Table 5. Properties of MgIIλ2800 emission line derived from parametric model fits (see Sect. 3.2).

ID	$\lambda_{50}^{\rm MgII}$ (Å)	$FWHM_{\rm MgII}$ (km s^{-1})	$EW_{\rm MgII}$ (Å)	$v_{50}^{\rm MgII}$ (km s^{-1})	Log ($L_{\rm MgII}$/erg s^{-1})	Log (L_{3000}/erg s^{-1})
X_N_160_22	2804 ± 1	3620 ± 180	25 ± 1	−390 ± 80	44.45 ± 0.07	46.46 ± 0.06
X_N_81_44	2801 ± 1	3910 ± 250	36 ± 2	−90 ± 100	44.37 ± 0.07	46.25 ± 0.06
X_N_53_3	2795 ± 1	2880 ± 290	17 ± 2	530 ± 120	44.18 ± 0.08	46.32 ± 0.06
X_N_66_23	2795 ± 3	3180 ± 880	26 ± 8	510 ± 340	43.70 ± 0.13	45.78 ± 0.07
X_N_4_48	2790 ± 4	8730 ± 1040	83 ± 14	1030 ± 380	44.27 ± 0.09	45.70 ± 0.07
X_N_102_35	2800 ± 1	4110 ± 190	23 ± 1	−2 ± 80	44.33 ± 0.07	46.40 ± 0.06
X_N_115_23	2803 ± 2	4320 ± 550	56 ± 8	−360 ± 210	44.12 ± 0.09	45.82 ± 0.07
cid_166	2803 ± 1	5910 ± 340	35 ± 2	−270 ± 140	44.64 ± 0.07	46.49 ± 0.06
cid_1605	2801 ± 1	4210 ± 420	42 ± 5	−150 ± 160	43.77 ± 0.08	45.50 ± 0.07
cid_346	2802 ± 2	5400 ± 660	29 ± 4	−220 ±250	44.03 ± 0.08	45.99 ± 0.06
cid_467	2801 ± 5	5830 ± 1340	17 ± 4	−60 ± 500	43.77 ± 0.11	45.95 ± 0.06
J1333+1649	2794 ± 1	3690 ± 80	12 ± 0	680 ± 30	45.15 ± 0.07	47.47 ± 0.06
J1441+0454	2792 ± 1	4010 ± 100	20 ± 0	880 ± 40	44.96 ± 0.07	47.05 ± 0.06
J1549+1245	2804 ± 1	3150 ± 70	22 ± 1	−410 ± 30	45.07 ± 0.07	47.15 ± 0.06
S82X1905	2805 ± 3	4430 ± 770	20 ± 4	−530 ± 330	43.93 ± 0.10	45.98 ± 0.06
S82X1940	2788 ± 2	3410 ± 500	370 ± 271	1240 ± 190	43.98 ± 0.09	43.63 ± 0.57
S82X2058	2792 ± 3	4490 ± 630	30 ± 4	910 ± 270	44.09 ± 0.09	46.09 ± 0.06

Notes. Columns give the following information for the BLR component of the MgII emission line: (1) target identification, (2) centroid (Å), (3) FWHM (km s^{-1}), (4) rest-frame EW (Å), (5) velocity of the MgII at 50% of the cumulative line flux, (6) logarithm of the extinction-corrected MgII luminosity, and (7) logarithm of the extinction-corrected luminosity at 3000 Å derived from the best-fit values of the power-law model representing the AGN continuum (see Sect. 3).

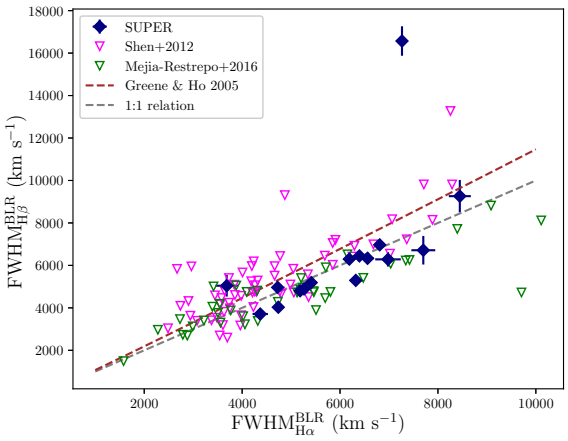

Fig. 5. Comparison between the FWHM of the BLR component of Hβ and Hα emission lines for the SUPER targets (blue diamonds). The SDSS sample from Shen & Liu (2012) and the sample from Mejía-Restrepo et al. (2016) are also shown (magenta and green triangles, respectively).

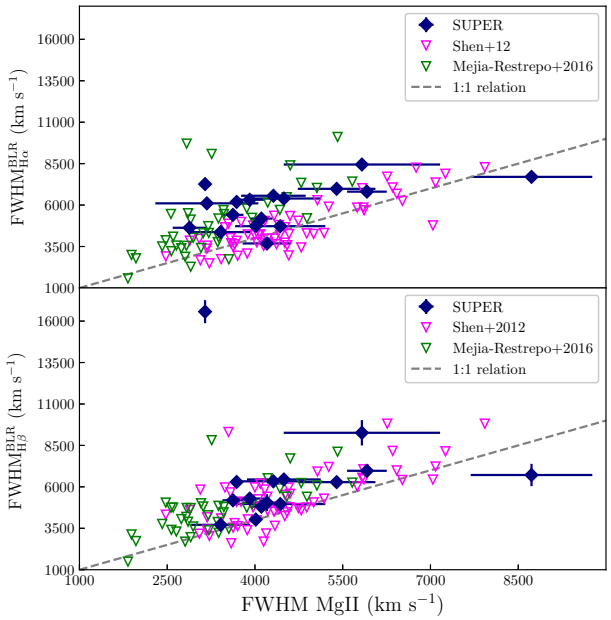

Fig. 6. FWHM of the BLR component of Hα (*upper panel*) and Hβ (*lower panel*) emission lines as a function of the FWHM of the MgII line for the SUPER targets (blue diamonds). The SDSS sample from Shen & Liu (2012) and the sample from Mejía-Restrepo et al. (2016) are also shown (magenta and green triangles, respectively).

4.3. Masses and Eddington ratios of SMBHs

As mentioned in Sect. 1, the BH mass can be estimated from single-epoch spectra assuming that the BLR is virialized. Based on the comparison of the FWHM for the broad lines observed (see Sect. 4.1), we estimate the virial BH mass from three of those emission lines: Hβ, Hα, and MgII. The virial BH mass calibration used for the broad Hβ line, available for 16 SUPER targets, is from Bongiorno et al. (2014):

$$\mathrm{Log}(M_{\rm BH}/M_\odot) = 6.7 + 2\times \mathrm{Log}\left(\frac{FWHM_{\rm H\beta}}{10^3\ \mathrm{km\,s^{-1}}}\right) + 0.5\times \mathrm{Log}\left(\frac{5100\,L_{5100}}{10^{44}\ \mathrm{erg\,s^{-1}}}\right) \quad (4)$$

where FWHM is the best-fit full width at half maximum of the broad component of Hβ and λL_λ is the best-fit extinction-corrected continuum luminosity at 5100 Å. This $M_{\rm BH}$(Hβ) is derived assuming $f = 1$.

The Greene & Ho (2005) calibration was used to derive the BH mass from the broad Hα, available for 21 SUPER targets:

Table 6. Spearman test results for the SUPER sample.

Correlation (1)	Slope (2)	ρ (3)	P-value (4)
FWHM Hβ vs. FWHM H$\alpha^{(1)}$	1.43 ± 0.49	0.88	6e−6
FWHM Hβ vs. FWHM H$\alpha^{(2)}$	0.95 ± 0.20	0.87	2e−5
FWHM Hβ vs. FWHM MgII$^{(1)}$	-0.05 ± 0.70	0.39	0.15
FWHM Hβ vs. FWHM MgII$^{(2)}$	2.89 ± 1.89	0.66	0.01
FWHM Hα vs. FWHM MgII$^{(1)}$	1.15 ± 0.63	0.41	0.11
FWHM Hα vs. FWHM MgII$^{(2)}$	0.63 ± 0.23	0.50	0.04
FWHM Hβ vs. FWHM CIV$^{(1)}$	-40.32 ± 0.14	−0.32	0.24
FWHM Hβ vs. FWHM CIV$^{(2)}$	-0.32 ± 0.14	−0.33	0.23
FWHM Hα vs. FWHM CIV	-0.13 ± 0.11	−0.15	0.54
Log $L_{H\alpha}$ vs Log L_{5100}	0.84 ± 0.05	0.79	6e−5
Log $L_{H\beta}$ vs Log L_{5100}	0.97 ± 0.06	0.94	6e−8
Log L_{1350} vs Log L_{5100}	0.78 ± 0.15	0.78	7e−5
Log L_{3000} vs Log L_{5100}	0.97 ± 0.19	0.86	2e−5
Log $L_{H\beta}$ vs Log $L_{H\alpha}$	1.09 ± 0.08	0.78	4e−4

Notes. We derived linear relations using the BCES (Y|X) regression (Akritas & Bershady 1996). Outlier objects showing a very broad FWHM of Hβ (J1549+1245, see Fig. 5) and MgII emission lines (X_N_4_48, see Sect. 6) have been included $^{(1)}$ and excluded $^{(2)}$ from the fit.

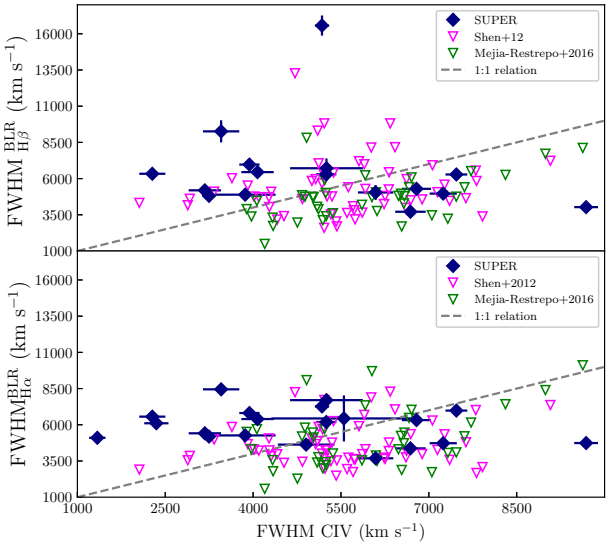

Fig. 7. FWHM of the BLR component of Hβ (*upper panel*) and Hα (*lower panel*) emission lines as a function of the FWHM of the CIV line for the SUPER targets. Symbols are the same as in Fig. 5.

$$\mathrm{Log}(M_{\mathrm{BH}}/M_{\odot}) = 6.3 + 2.06 \times \mathrm{Log}\left(\frac{FWHM_{\mathrm{H}\alpha}}{10^3\,\mathrm{km\,s^{-1}}}\right) + 0.55 \times \mathrm{Log}\left(\frac{L_{\mathrm{H}\alpha}}{10^{42}\,\mathrm{erg\,s^{-1}}}\right) \quad (5)$$

with the best-fit value of the FWHM of the profile of Hα line and extinction-corrected Hα luminosity $L_{\mathrm{H}\alpha}$.

We used the Bongiorno et al. (2014) calibrated formula for the MgII emission line, available for 17 SUPER targets:

$$\mathrm{Log}(M_{\mathrm{BH}}/M_{\odot}) = 6.6 + 2 \times \mathrm{Log}\left(\frac{FWHM_{\mathrm{MgII}}}{10^3\,\mathrm{km\,s^{-1}}}\right) + 0.5 \times \mathrm{Log}\left(\frac{3000\,L_{3000}}{10^{44}\,\mathrm{erg\,s^{-1}}}\right) \quad (6)$$

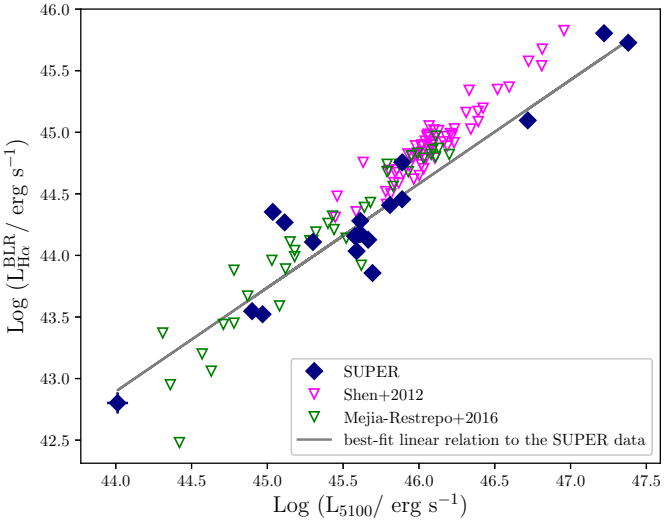

Fig. 8. Comparison between the continuum luminosity at 5100 Å derived from the best-fit continuum power-law model with the luminosity of the broad Hα emission line, both in logarithmic scale, for the SUPER sample (blue circles). Both continuum and emission line luminosities are corrected for extinction (see Sect. 4.2). The SDSS sample from Shen & Liu (2012) and the sample from Mejía-Restrepo et al. (2016) are also shown (red and green circles, respectively). The best-fit linear relation (BCES Y|X regression) for the SUPER data is shown as a grey solid line.

with the best-fit value of the FWHM of the profile of MgII line and extinction-corrected luminosity λL_{λ} at 3000 Å.

Mejía-Restrepo et al. (2018) found a relation between the virial factor f and the width of the broad lines:

$$f = \left(\frac{FWHM_{\mathrm{obs}}(\mathrm{line})}{FWHM^{0}_{\mathrm{obs}}}\right)^{\beta}, \quad (7)$$

where $FWHM_{\mathrm{obs}}$(line) is the observed FWHM of a broad line, Hα, Hβ, and MgII in our case, with $FWHM^{0}_{\mathrm{obs}} = 4000 \pm 700$ and $\beta = -1.00 \pm 0.10$ for the Hα line, $FWHM^{0}_{\mathrm{obs}} = 4500 \pm 1000$ and $\beta = -1.17 \pm 0.11$ for the Hβ line, and $FWHM^{0}_{\mathrm{obs}} = 3200 \pm 800$ and $\beta = -1.21 \pm 0.24$ for the MgII line.

We derived this virial factor f for Hα, Hβ, and MgII. The mean values are $f = 0.77 \pm 0.20$, $f = 0.70 \pm 0.12$, and $f = 0.74 \pm 0.23$ for Hβ, Hα, and MgII, respectively, justifying the assumption of $f = 1$ in Eqs. (4)–(6).

Regarding CIV-derived masses, this cannot be used to estimate BH mass due to the non-virialized CIV-emitting gas motion discussed earlier. The Hβ-based, Hα-based, and MgII-based BH masses are listed in Table 7. The values of the BH mass of the SUPER sample derived from Hα and Hβ lines are in relative agreement as shown in Fig. 9. The SDSS AGNs from the Shen & Liu (2012) and Mejía-Restrepo et al. (2016) samples are also plotted[5]. A correlation is also found between the Balmer-based and MgII-based BH masses (see Fig. 10), however the MgII line profile is affected by strong sky-line residuals in almost all spectra of the SUPER AGNs, which can affect the measured line properties and hence the derived BH mass.

As fiducial virial BH masses, we used the values derived from the Hβ emission lines, which we prefer over the Hα line

[5] We derived the BH mass of Shen & Liu (2012) and Mejía-Restrepo et al. (2016) samples by using Eqs. 4–(6) and the Eddington ratio from Eq. (8).

Table 7. Hβ-based, Hα-based, and MgII-based SMBH mass, Hβ-based and Hα-based Eddington ratio of the SUPER AGNs (see Sect. 4.3 for details).

ID	Log ($M_{\rm BH}^{\rm H\beta}/M_\odot$)	Log ($M_{\rm BH}^{\rm H\alpha}/M_\odot$)	Log($M_{\rm BH}^{\rm MgII}/M_\odot$)	$\lambda_{\rm Edd}^{\rm H\beta}$	$\lambda_{\rm Edd}^{\rm H\alpha}$
(1)	(2)	(3)	(4)	(5)	(6)
X_N_160_22	9.07 ± 0.30	9.16 ± 0.30	8.95 ± 0.30	0.31 ± 0.21	0.25 ± 0.17
X_N_81_44	9.05 ± 0.30	9.28 ± 0.30	8.91 ± 0.31	0.37 ± 0.26	0.22 ± 0.15
X_N_53_3	–	8.53 ± 0.30	8.68 ± 0.31	–	0.32 ± 0.22
X_N_66_23	–	8.94 ± 0.30	8.49 ± 0.39	–	0.08 ± 0.06
X_N_35_20	–	8.41 ± 0.38	–	–	0.07 ± 0.06
X_N_12_26	8.87 ± 0.30	8.91 ± 0.30	–	0.30 ± 0.21	0.27 ± 0.19
X_N_44_64	–	8.76 ± 0.31	–	–	0.04 ± 0.03
X_N_4_48	8.91 ± 0.31	9.37 ± 0.30	9.33 ± 0.32	0.12 ± 0.09	0.04 ± 0.03
X_N_102_35	8.85 ± 0.30	8.96 ± 0.30	9.03 ± 0.30	0.62 ± 0.43	0.48 ± 0.34
X_N_115_23	9.11 ± 0.30	9.24 ± 0.30	8.78 ± 0.32	0.16 ± 0.11	0.12 ± 0.08
cid_166	9.33 ± 0.30	9.53 ± 0.30	9.39 ± 0.31	0.26 ± 0.18	0.17 ± 0.12
cid_1605	8.55 ± 0.31	8.32 ± 0.31	8.60 ± 0.31	0.20 ± 0.14	0.34 ± 0.24
cid_346	9.13 ± 0.30	9.21 ± 0.30	9.06 ± 0.32	0.23 ± 0.16	0.19 ± 0.13
cid_1205	–	8.60 ± 0.30	–	–	0.10 ± 0.07
cid_467	9.28 ± 0.31	9.37 ± 0.30	9.11 ± 0.36	0.12 ± 0.08	0.10 ± 0.07
J1333+1649	9.99 ± 0.30	9.98 ± 0.30	9.47 ± 0.30	0.56 ± 0.39	0.57 ± 0.39
J1441+0454	9.27 ± 0.30	9.40 ± 0.30	9.33 ± 0.30	1.27 ± 0.88	0.95 ± 0.66
J1549+1245	10.75 ± 0.30	10.17 ± 0.30	9.17 ± 0.30	0.06 ± 0.04	0.24 ± 0.17
S82X1905	8.90 ± 0.30	8.89 ± 0.30	8.89 ± 0.34	0.27 ± 0.18	0.27 ± 0.19
S82X1940	8.36 ± 0.30	8.91 ± 0.30	7.48 ± 0.43	0.31 ± 0.22	0.09 ± 0.06
S82X2058	9.12 ± 0.30	9.16 ± 0.30	8.95 ± 0.33	0.12 ± 0.09	0.11 ± 0.08

Notes. Columns give the following information: (1) target identification, (2) logarithm of Hβ-based BH mass, (3) logarithm of Hα-based BH mass, (4) logarithm of MgII-based BH mass, (5) Eddington ratio derived from Hβ-based BH mass and (6) Eddington ratio derived from Hα-based BH mass. The error associated with the BH masses and hence Eddington ratios includes both the statistical uncertainties affecting the continuum or line luminosities and FWHM values and the systematic uncertainty in the virial relations (~0.3 dex, e.g. Bongiorno et al. 2014).

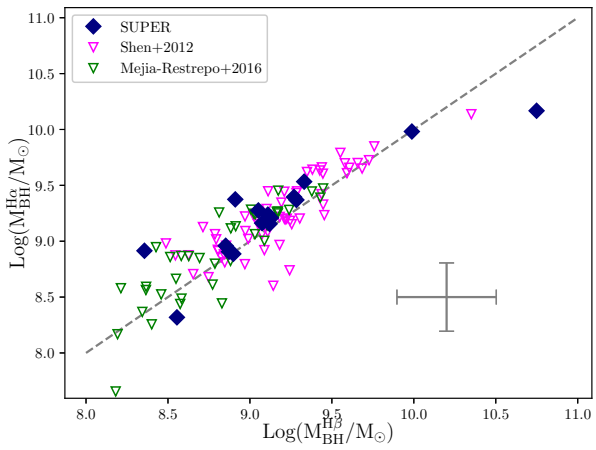

Fig. 9. Hα BH mass as a function of Hβ BH mass, both in logarithmic scale, for the SUPER targets (blue points) and SDSS targets from Shen & Liu (2012) (blue points). The 1:1 relation is shown as a dashed line. The typical uncertainty on the Hα- and Hβ-based BH masses for the SUPER sample is also represented in the bottom right-hand corner.

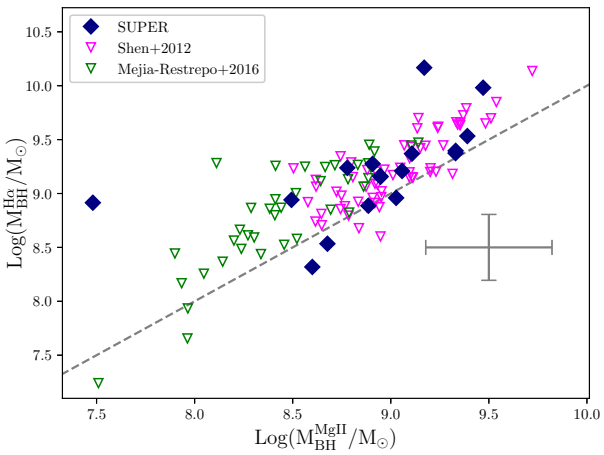

Fig. 10. Hα BH mass as a function of MgII BH mass, both in logarithmic scale, for the SUPER targets (blue points) and SDSS targets from Shen & Liu (2012) (blue points). The 1:1 relation is shown as dashed line. The typical uncertainty on the Hα- and MgII-based BH masses for the SUPER sample is also represented in the bottom right-hand corner.

because the latter is blended with the [NII]$\lambda\lambda$ 6548,6583 doublet implying a less reliable measurement. For five SUPER targets (i.e. X_N_53_3, X_N_66_23, X_N_35_20, X_N_44_64 and cid_1205), we used the BH mass values derived from Hα, because the Hβ line is not detected in those sources.

We found that the SUPER sample hosts BHs with log $M_{\rm BH} = 8.4$–$10.8\,M_\odot$. From the BH mass and the bolometric luminosity derived from the SED fitting (see Circosta et al. 2018), we derived the Eddington ratio for a solar composition gas, defined as:

$$\lambda_{\rm Edd} = \frac{L_{\rm Bol}}{1.5 \times 10^{38} M_{\rm BH}}. \quad (8)$$

We find values in the range $\lambda_{\rm Edd} = 0.04$–1.3 (see Table 7).

Figure 11 shows the comparison of $M_{\rm BH}$, $L_{\rm Bol}$, and $\lambda_{\rm Edd}$ measured for the SUPER sample with those derived from a sample

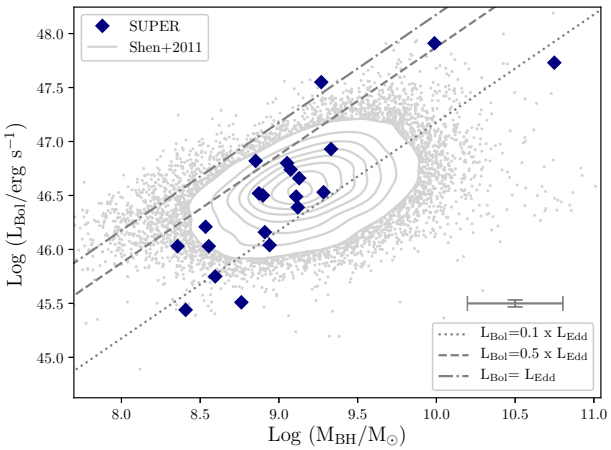

Fig. 11. Bolometric luminosity as a function of BH mass, both in logarithmic scale, for the SUPER sample. Luminosity in fractions of 0.1, 0.5, and 1 Eddington luminosity are respectively indicated with dot-dashed, dotted, and dashed lines. Contours and grey points refer to SDSS DR7 QSOs from Shen et al. (2011).

of ~23 000 SDSS AGNs at $1.5 \leq z \leq 2.2$ with MgII-based BH mass (Shen et al. (2011), contour lines). The bolometric luminosity in fractions of 0.1, 0.5, and 1 Eddington luminosity is also reported. The SUPER sample spans two orders of magnitude in bolometric luminosity and in Log ($M_{BH}/M_\odot$).

5. Broad line region winds

5.1. Connection between CIV velocity shift and AGN properties

As discussed in Sect. 4.1, the FWHM of the CIV line does not correlate with those of the Balmer lines, suggesting a different kinematical state for the gas traced by the CIV emission. Indeed, this line is known to be dominated by non-virialized motion components, making the profile asymmetric towards the blue-side of the line (e.g. Gaskell 1982, Richards et al. 2011). While this is a limitation on the use of such a line for measuring BH masses, it offers the opportunity to trace the motion of the ionised gas in the BLR (e.g. Vietri et al. 2018). To achieve this goal, we measured the velocity shift of the CIV with respect to the expected wavelength based on [OIII] systemic redshift, which is defined as $v_{50}^{CIV} = c \times (\lambda_{half} - 1549.48)/1549.48$, where λ_{half} is the wavelength that bisects the cumulative total line flux, and c the speed of light. In Fig. 12 we can see that 85% of the SUPER objects have a CIV velocity shift <~2000 km s^{-1} and equivalent width (EW) ≥18 Å up to ~80 Å and 15% have velocity larger than 2000 km s^{-1} up to ~4700 km s^{-1} and an $EW_{CIV} \sim$ 20–30 Å. The WISSH targets presented in Vietri et al. (2018) are also shown in Fig. 12 to probe the high-end of luminosity distribution ($L_{Bol} > 10^{47}$–10^{48} erg s^{-1}). Overall, we confirm with our sample the same anti-correlation between the EW and the velocity shift of the CIV line previously reported in the literature (e.g. Sulentic et al. 2007; Richards et al. 2011: Vietri et al. 2018).

In Vietri et al. (2018) we reported a strong dependence of the velocity shift of the CIV emission line on physical parameters such as bolometric luminosity and optical-to-X-ray spectral slope (α_{OX}), as well as Eddington ratio, despite the non-homogeneous parametrisation of bolometric luminosity, BH mass, and the CIV velocity shift of the collected dataset (WISSH and samples from the literature). Here, we further investigate these correlations, this time with the advantage conferred by an

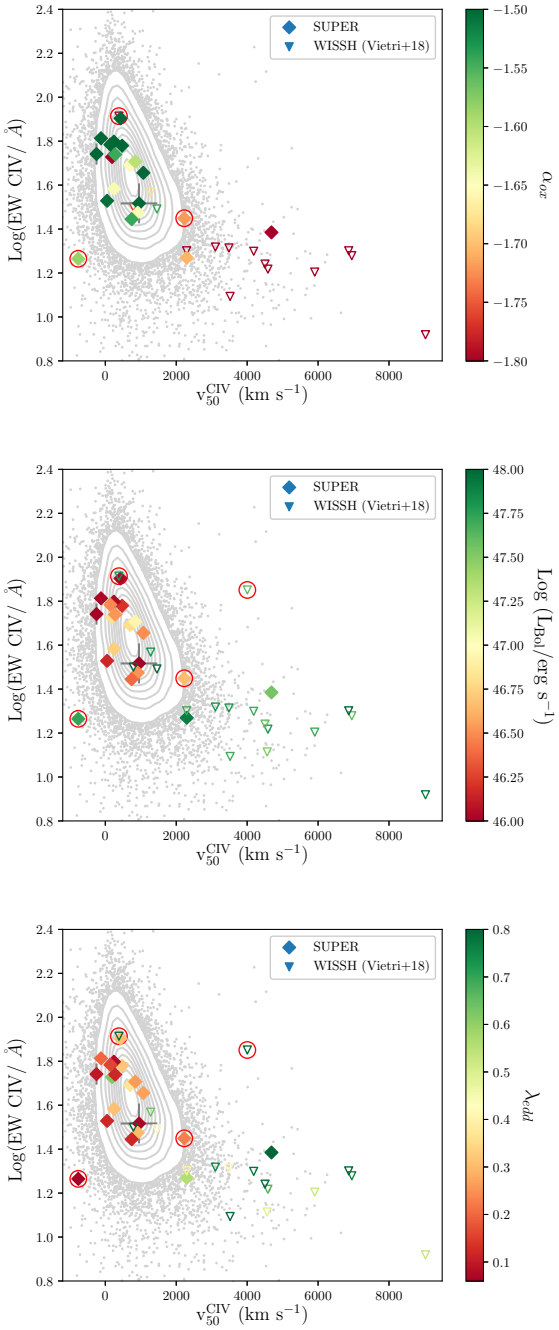

Fig. 12. Logarithm of EWs as a function of the velocity shift of the CIV emission line for the SUPER sample (diamonds), colour-coded according to the α_{OX} (*top*), L_{Bol} (*middle*), and λ_{Edd} (*bottom*). Additionally, the SDSS sample from Shen et al. (2011) (contours and grey points) and the WISSH sample from Vietri et al. (2018) (open triangles) are also reported. BAL AGNs are indicated with red circles.

unbiased sample such as SUPER, covering two orders of magnitude in bolometric luminosity and a wide range of BH masses and Eddington ratios. We also populate the high-luminosity range by adding the Type-1 AGNs from the WISSH survey[6] (Vietri et al. 2018) to the SUPER sample. We computed α_{OX}

[6] The bolometric luminosities of the WISSH QSOs are derived from SED-fitting as reported in Duras et al. (2017), and the BH mass and Eddington ratio are derived using Eqs. (4) and (8). For the α_{OX} we used the values reported in Martocchia et al. (2017) and Zappacosta et al. (2020).

for each of our SUPER quasars following the definition:

$$\alpha_{ox} = \frac{\mathrm{Log}(L_{2\,\mathrm{Kev}}/L_{2500\,\text{Å}})}{\mathrm{Log}(\nu_{2\,\mathrm{Kev}}/\nu_{2500})}, \quad (9)$$

where L_{2500} and $L_{2\,\mathrm{keV}}$ are the restframe monochromatic luminosities at 2500 Å and 2 keV. For the calculation of α_{OX} we used the rest-frame 2500 Å monochromatic luminosity obtained by SED fitting (Circosta et al. 2018) and derived the $L_{2\,\mathrm{keV}}$ assuming $L_{2-10\,\mathrm{keV}} = 1.61 \times L_{2\,\mathrm{keV}}$, adopting a power-law X-ray model with $\Gamma = 2$. As shown in the three panels of Fig. 12 there is indeed a strong correlation between the v_{50}^{CIV} with all three of the above mentioned physical quantities: bolometric luminosity, Eddington ratio, and α_{OX}. In particular, in the top panel of Fig. 12 the data points in the plane of EW_{CIV} versus v_{50}^{CIV} are colour-coded according to the α_{OX} values: most of the SUPER sources with $v_{50}^{CIV} < 2000\,\mathrm{km\,s^{-1}}$ have $\alpha_{OX} > -1.6$, while the WISSH targets, which are sampling the high-luminosity end of the quasar population, have mostly lower values of α_{OX}. This parameter can be used as a measurement of the hardness of the ionising SED, whereby larger values of α_{OX} corresponds to large amounts of ionising radiation for a given optical-UV luminosity. In the context of a disc-wind scenario, this behaviour suggests that the objects with harder SEDs produce larger amounts of high-ionisation gas, which means higher values of CIV EW. If the ionising radiation overionises the gas, the continuum-driving (bound-free absorption) mechanism becomes inefficient, which could explain the smaller velocity shift of the CIV. Instead, 15% of the sources of the SUPER sample (and the WISSH quasars), which show softer SEDs, produce high-velocity BLR winds ($v_{50}^{CIV} > 2000\,\mathrm{km\,s^{-1}}$). Therefore, the acceleration is probably correlated with the hardness of the ionising continuum, the ionisation parameter, and α_{OX}, but more specific calculations are required to demonstrate these connections.

In the medium and bottom panels of Fig. 12, the plane of EW_{CIV} versus v_{50}^{CIV} is colour-coded according to the bolometric luminosity and Eddington ratio, respectively. SUPER sources with $v_{50}^{CIV} < 2000\,\mathrm{km\,s^{-1}}$ have luminosity range $\log(L_{Bol}/\mathrm{erg\,s^{-1}}) = 45.4$–$46.9$, with the exception of one BAL source, J1549+1245, which has $\mathrm{Log}(L_{Bol}/\mathrm{erg\,s^{-1}}) = 47.7$, and $v_{50}^{CIV} > 2000\,\mathrm{km\,s^{-1}}$ in the range $\log(L_{Bol}/\mathrm{erg\,s^{-1}}) = 46.7$–$47.9$. The high-velocity-shift end is also strongly populated by the WISSH sample, with $\log(L_{Bol}/\mathrm{erg\,s^{-1}}) > 47$. On the other hand, SUPER sources with $v_{50}^{CIV} < 2000\,\mathrm{km\,s^{-1}}$ have Eddington ratios in the range 0.06–0.62 with a median value of 0.18, while for the high-velocity winds the range is 0.23–1.27 with a median value of 0.56. We computed the Spearman's rank correlation coefficient, ρ, and associated p-value to quantify the strength and significance of each correlation, considering both SUPER and WISSH samples. We focused on the sources with reliable CIV velocity shift, and therefore we excluded the source J1549+1245, whose peak and half of the profile are totally absorbed by the presence of a BAL. We find that the v_{50}^{CIV} correlates with α_{OX} with a coefficient $\rho = -0.79$ and p-value $< 10^{-5}$ (taking into account upper limits using the Astronomical Survival Analysis (ASURV) package available under IRAF/STSDAS; Lavalley et al. 1992, Feigelson & Nelson 1985, Isobe et al. 1986), with Log L_{Bol} with a coefficient $\rho = 0.64$ and p-value $= 2 \times 10^{-5}$ and with λ_{Edd} with a coefficient $\rho = 0.62$ and a p-value $= 5 \times 10^{-5}$. These values confirm the visual impression given by Fig. 12 that the properties of the CIV line correlate with all three of these parameters, but the highest significant correlation is with α_{OX}. Recently, Zappacosta et al. (2020), studying the WISSH sources, reported

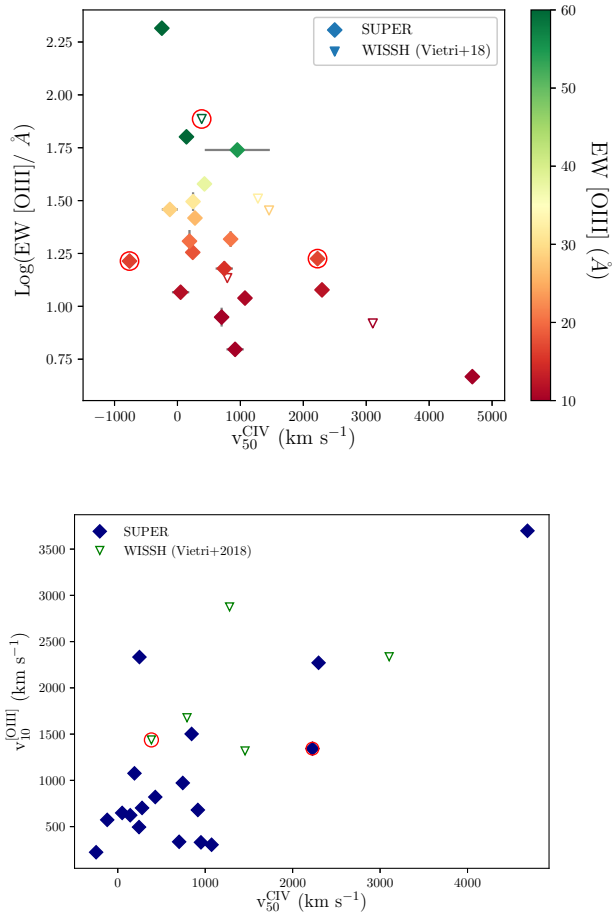

Fig. 13. *Top*: [OIII] EW in logarithm as a function of the velocity shift of the CIV emission line for the SUPER sample (diamonds), colour-coded according to the $EW_{[OIII]}$. Additionally, the WISSH sample with reliable [OIII] measurements is also reported (empty triangles). *Bottom*: velocity of [OIII] at 10% of the line flux as a function of the velocity shift of the CIV emission line for the SUPER sample (blue diamonds). The WISSH subsample with reliable [OIII] measurements is also shown as green triangles. BAL AGNs are indicated with red circles.

a significant correlation between the luminosity in the 2–10 keV band ($L_{2-10\,\mathrm{keV}}$) and the blueshift of the CIV line, that is, objects exhibiting a high-velocity shift have lower $L_{2-10\,\mathrm{keV}}$. With the SUPER sample we are not able to properly investigate this relation. Indeed, the narrow velocity range spanned by the SUPER sample (compared to the wide range probed by the WISSH sample; see Fig. 12), which can possibly depend on L_{Bol} (e.g. Fiore et al. 2017), would require a much larger number of sources in order to place significant constraints on a possible existing correlation at lower luminosities.

While we are using CIV to trace the AGN winds in the BLR, the main aim of our survey is to trace the AGN-driven outflows in the NLR using the [OIII] line (Kakkad et al. 2020). It is therefore interesting to compare the properties of the winds traced at such different physical scales. In Fig. 13, it is shown the [OIII] EW as a function of v_{50}^{CIV}. The strength of the [OIII] seems to decrease with increasing CIV velocity shift, that is, for $v < 2000\,\mathrm{km\,s^{-1}}$ the EW[OIII] range probed is 6–207Å with a mean (median) value of 36(21) Å and for $v > 2000\,\mathrm{km\,s^{-1}}$ the range is 5–17 Å with a mean(median) value of 11(12) Å. Furthermore, we also compare the kinematic properties of the CIV and [OIII] emission lines. We used the non-parametric definition v_{10}, that is, the

velocity of the [OIII] at 10% of the cumulative line flux, to trace the [OIII] outflow velocity (see Kakkad et al. 2020).

We find a significant correlation between $v_{10}^{[OIII]}$ and the CIV blueshift, with a Spearman correlation coefficient $\rho = 0.54$ and p-value $= 0.007$[7]. We also test for the presence of a correlation between v_{50}^{CIV} and W_{80} (the width containing 80% of the line flux), and between v_{50}^{CIV} and v_{max} (defined as the shift between the systemic velocity and the broad Gaussian component of [OIII] plus twice the velocity dispersion of the broad Gaussian). In our analysis of the NLR winds we use a cut of W_{80} larger than 600 km s^{-1} to distinguish between targets with and without AGN outflows (Kakkad et al. 2020). In this case we report a marginally significant correlation with W_{80}, with $\rho = 0.42$ and p-value $= 0.05$, and a weaker and non-significant correlation with v_{max}, with $\rho = 0.32$ and p-value $= 0.13$.

Our findings are in agreement with those presented by Coatman et al. (2019), despite the lower statistical significance of our correlations which is likely due to the smaller sample. These latter authors analysed the integrated spectra of 213 quasars in the luminosity range of Log $(L_{Bol}/\mathrm{erg\,s^{-1}}) = 46$–$49$ with redshift $z \sim 2$–4 and found a significant correlation (p-value $= 6 \times 10^{-7}$) between v_{10} and v_{50}^{CIV} with $\rho = 0.46$. They demonstrated that the correlation is independent of the bolometric luminosity; however we note that both $v_{10}^{[OIII]}$ and v_{50}^{CIV} correlate with bolometric luminosities for the SUPER and WISSH samples, although with a large scatter. While the analysis of Coatman et al. (2019) was limited by the lack of spatially resolved data to locate the scale over which the gas traced by the [OIII] emission was located, we inferred from the SINFONI IFU data that the [OIII] emission is extended over kiloparsec scales (Kakkad et al. 2020), therefore supporting the idea that BLR outflows may affect the gas at galaxy-scale distances in the ISM.

5.2. Outflow energetics

Our estimate of the ionised gas mass, M_{out}, is somewhat different from that used in Vietri et al. (2018) which followed the expression given in Marziani et al. (2016). The approximation in Vietri et al. (2018) was based on a spherical gas distribution and did not take into account the dependence on the gas temperature. Here we assume a thin-shell geometry for the outflowing gas and normalise the results using photoionisation calculations typical of BLR conditions.

The expression we use for the CIV line is similar to the one given in Baron & Netzer (2019), and in several earlier publications for the [OIII] line. It assumes a line emission coefficient, γ_{CIV} ($L_{line} \propto \gamma n_e^2$) given by:

$$\gamma_{CIV} = C_{CIV} \times h\nu_{CIV} \frac{n(C^{+3})}{n(C)} \frac{n(C)}{n(H)}, \quad (10)$$

where $C_{CIV} \propto \exp\left[\frac{-h\nu}{kT}\right] / \sqrt{T}$, and $n(C^{+3})/n(C)$ is the fractional ionisation of C^{+3}. The line luminosity is obtained by integrating the emissivity over volume and the associated mass is $M_{out} \propto L(CIV)/n_e\gamma_{CIV}$.

Using known atomic rates, and calibrating the above expressions against photoionisation calculations (see e.g. the specific calculations in Netzer 2020) of a thin shell of gas with constant density, we get:

$$M_{out} \approx 100 \frac{L_{45}(CIV)}{n_9 \times n(C^{+3})/n(C)} M_\odot, \quad (11)$$

where n_9 is the electron density in units of 10^9 cm^{-3} and $L_{45}(CIV)$ is the CIV luminosity in units of 10^{45} erg s^{-1}. This estimate is appropriate for the highly ionised part of the cloud, and for 1.5×10^4 K $< T < 2 \times 10^4$ K and metallicity in the range of one to five times solar. To derive the mass of the wind we used the CIV luminosity of the total profile based on the fact that the bulk of our sources show blue-asymmetry according to the CIV shifts.

It is important to note that higher metallicity $(n(C))/n(H))$ tends to cool the gas which compensates for much of the influence of the temperature on the excitation rate. Thus, the main dependence is on the fractional ionisation which is determined by the ionisation parameter and not on the carbon abundance. This is why the carbon abundance term is not part of the mass equation.

The fractional ionisation of carbon scales with the hydrogen ionisation parameter, U, and depends also on the metallicity through the gas temperature. For $U = 0.05$, $n(C^{+3})/n(C) \simeq 0.5$. The mass obtained here is about an order of magnitude smaller than the one obtained by using the Marziani et al. (2016) expression. We derived the following range of outflowing mass: $M_{out} = 0.1$–$290\,M_\odot$, assuming $n = 10^{9.5}$ cm^{-3}.

For the mass outflow rate we use the expression for a thin outflowing shell,

$$\dot{M}_{out} = M_{out} \frac{v}{r_{CIV}} \approx 0.005 M_{out} \frac{v_{5000}}{r_{pc}} M_\odot\,\mathrm{yr}^{-1}, \quad (12)$$

where v_{5000} is the outflow velocity[8] v_{50}^{CIV} in 5000 km s^{-1} and r_{CIV} is the outflow radius estimated from the CIV radius-luminosity relation from Lira et al. (2018).

The inferred outflow radius $R \sim 0.002$–0.2 pc is listed in Table 8 along with the mass outflow rates: $\dot{M}_{out} = 0.005$–$3\,M_\odot$ yr^{-1} with a mean value $0.4\,M_\odot$ yr^{-1}. This is a factor of three smaller than the one used in Vietri et al. (2018) for a spherical geometry.

The two main uncertainties in the above mass and mass outflow rate estimates are the unknown gas density and level of ionisation. A lower limit on the density is imposed from the very different shape of the C III]1909 line profile which does not show a blueshifted wing and similarly from other semi-forbidden lines like O III]1664 (e.g. Richards et al. 2011, Netzer 2013). This limit is about 3×10^9 cm^{-3}. The upper limit is more difficult to establish. Photoionisation calculations (Netzer 2013) suggest several other strong broad lines, like NVλ1240, which will show blueshifted wings under such conditions. Nevertheless, we lack high-quality spectra for these lines. In Eq. (11) we used $n_e = 10^{9.5}$ cm^{-3}. As for the level of ionisation of the outflowing gas, this can be high and results in little C^{+3}, and will increase both M_{out} and $\dot{M}_{out}$. Finally, without proper modelling, we lack information about the amount of neutral gas that can be part of the outflow. Such gas will increase both M_{out} and $\dot{M}_{out}$.

In Fig. 14 we plot the derived mass outflow rate of the CIV winds as a function of the bolometric luminosity for the SUPER sample. We also include the WISSH sample to populate the high-luminosity part and added the correlation of mass

[7] The probability of the correlation decreases if we exclude from the fit the only object showing $v_{50}^{CIV} > 3500$ km s^{-1} and $v_{10}^{[OIII]} > 3000$ km s^{-1}, i.e. $\rho = 0.48$ and p-value $= 0.02$.

[8] The calculations of the maximum velocity of the outflow require numerical integration across the BLR and a point-by-point calculation of the force multiplier (see Netzer 2013 Chapter 5.9.2). This is beyond the scope of the present work.

Table 8. Properties of the CIV outflows derived from the total profile of the CIV emission line.

ID	v_{peak}^{CIV}	R	v_{50}^{CIV}	M_{out}	$\dot{M}_{out}$	Log($\dot{E}_{kin}$/erg s^{-1})	Log($\dot{P}_{out}$/g cm s^{-2})
(1)	(2)	(3)	(4)	(5)	(6)	(7)	(8)
	km s^{-1}	pc	km s^{-1}	$M_\odot$	$M_\odot$ yr^{-1}		
X_N_160_22	−30	0.06	250	68.46	0.10	39.31	32.21
X_N_81_44	700	0.04	700	37.37	0.26	40.60	33.06
X_N_53_3	540	0.03	470	29.40	0.17	40.07	32.69
X_N_66_23	110	0.02	240	14.14	0.06	39.02	31.93
X_N_35_20	950	0.01	950	2.31	0.06	40.23	32.55
X_N_12_26	430	0.04	920	19.43	0.17	40.66	33.00
X_N_4_48	260	0.03	50	16.28	0.01	36.87	30.47
X_N_102_35	400	0.06	190	87.51	0.11	39.09	32.11
X_N_115_23	70	0.04	140	38.84	0.05	38.51	31.66
cid_166	780	0.06	850	109.30	0.52	41.07	33.45
cid_1605	−120	0.02	−120	12.64	0.03	38.07	31.29
cid_346	2230	0.05	2230	28.72	0.50	41.89	33.85
cid_1205	−250	0.002	−250	0.14	0.005	37.98	30.88
cid_467	210	0.05	280	51.23	0.11	39.42	32.28
J1333+1649	2160	0.15	2300	285.46	1.56	42.42	34.36
J1441+0454	3320	0.11	4690	189.15	2.85	43.29	34.93
S82X1905	1070	0.04	1070	27.36	0.30	41.03	33.30
S82X1940	430	0.02	430	16.40	0.11	39.81	32.47
S82X2058	680	0.05	740	25.86	0.16	40.44	32.87

Notes. Columns give the following information: (1) target identification, (2) the velocity at the peak of the CIV total profile, (3) CIV BLR radius derived from the CIV radius-luminosity relation from Lira et al. (2018), (4) velocity of the CIV at 50% of the cumulative line flux, (5) mass of the outflow ($M\odot$), (6) mass outflow rate assuming a thin-shell geometry as described in Sect. 5.2, (7) kinetic power of the outflow and (8) outflow momentum load.

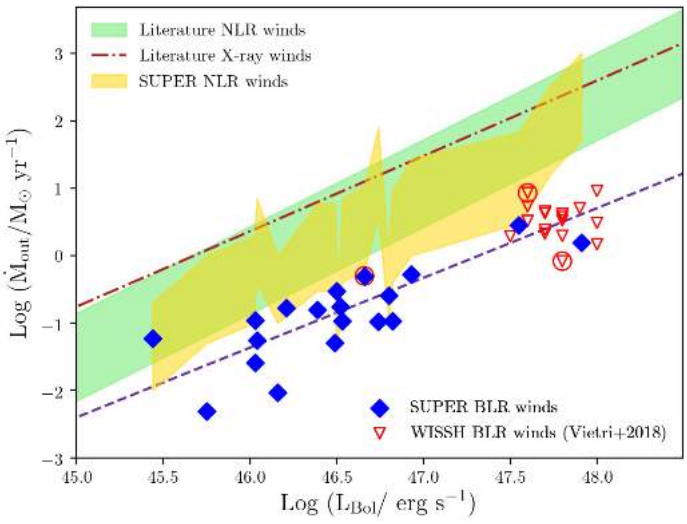

Fig. 14. Outflow mass rate as a function of the logarithm of the bolometric luminosity for the BLR winds in the SUPER sample. Values from the WISSH sample (Vietri et al. 2018) (triangles) are also reported. BAL AGNs are denoted with red circles. The blue dashed line is the best-fit correlation of the CIV winds (SUPER+WISSH samples). Mass outflow rates of NLR winds from the SUPER sample are also reported (gold shaded area). The green shaded area shows the range probed by the outflow ionised phase in the NLR as found by Fiore et al. (2017), after rescaling the relation with the same assumption as for the Type-1 SUPER targets (see Kakkad et al. 2020 for further details). The dot-dashed line shows the log linear best-fit correlation of the X-ray winds.

outflow rate versus bolometric luminosity from a compilation of ionised and X-ray winds (see Fiore et al. 2017). For the BLR, $\dot{M}_{out}$, and L_{bol} we derive a Spearman correlation coefficient $\rho = 0.8$ and null hypothesis $P = 1 \times 10^{-8}$, with a log linear slope Log $(\dot{M}_{out}/M_\odot\,\mathrm{yr}^{-1}) \propto 1.01 \pm 0.09\,\mathrm{Log}(L_{Bol}/\mathrm{erg\,s}^{-1})$. Interestingly, the mass-outflow rates of the BLR winds seem to show a correlation with the bolometric luminosity of the central AGN that is as steep as that observed for the ionised winds in the NLR and X-ray-traced winds close to the accretion disk. The different normalization could be due to the efficiency of the coupling with the ISM, which changes in terms of density and composition, but a similar slope suggests that the winds at different scales are linked, or more specifically that they have the same functional dependency on a basic physical property of the SMBH, its bolometric luminosity.

The $\dot{M}_{out}$ values inferred for the BLR winds are lower than the ones derived for X-ray winds. Further, the range probed by the BLR winds in terms of mass outflow rate is lower than that of the NLR winds measured for the 18 objects for which we can sample both regions (see also Kakkad et al. 2020 for the [OIII] analysis). In Fig. 14 we plot the mass outflow rates for the SUPER NLR winds assuming a bi-conical outflow model and an electron density from 500 cm^{-3} to 10 000 cm^{-3}, as reported in Kakkad et al. (2020). For 6 of these 18 objects, the mass outflow rates of the BLR winds are consistent with the lower limit found from the NLR analysis.

We also estimated the kinetic power of the outflow defined as:

$$\dot{E}_{kin} = \frac{1}{2}\dot{M}_{out}v_{out}^2, \tag{13}$$

with $v_{out} = v_{50}^{CIV}$ and $\dot{M}_{out}$ as derived in Eq. (12). We derived $\dot{E}_{kin}$ from 7.4×10^{36} erg s^{-1} up to 2×10^{43} erg s^{-1} for the SUPER object with the most blueshifted CIV line profile, namely J1441+0454.

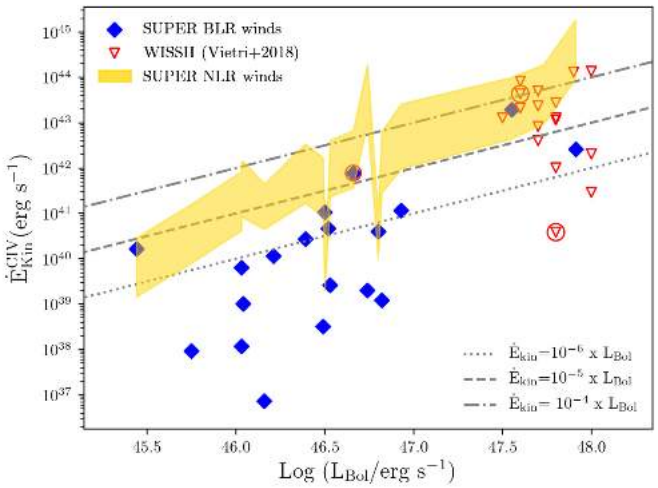

Fig. 15. Kinetic power of the BLR winds as a function of the logarithm of the bolometric luminosities for the SUPER sample (diamonds). Values of the BLR winds from the WISSH sample (Vietri et al. 2018) (triangles) are also reported. The kinetic power of NLR winds from the SUPER sample is reported (gold shaded area). Kinetic power in fractions of 10^{-4}, 10^{-5}, and 10^{-6} bolometric luminosity are respectively indicated with dot-dashed, dashed, and dotted lines. BAL sources are denoted with red circles.

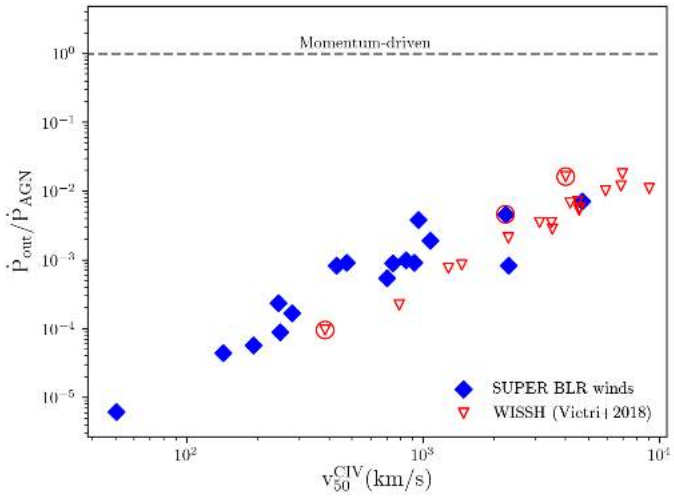

Fig. 16. Outflow momentum load as a function of the velocity shift of the CIV for the SUPER sample (blue diamonds). The WISSH sample is also reported as red triangles. The dashed line indicates the theoretical expectation for a momentum-driven outflow. BAL sources are denoted with red circles.

Figure 15 shows the kinetic power derived using the CIV total profile as a function of bolometric luminosity for the SUPER sample (diamonds). We also populated the high-luminosity part of the plot, adding the values estimated in a consistent way for the WISSH sample. Performing a Spearman test on $\dot{E}_{\rm kin}$ and $L_{\rm Bol}$ for both samples, the quantities are strongly correlated with a log linear slope of 2.14 ± 0.25 and a Spearman correlation coefficient $\rho \sim 0.74$ and two-sided null hypothesis of $p = 3 \times 10^{-7}$. The bulk of the kinetic power for the BLR winds in the SUPER sample is in the range $\dot{E}_{\rm kin} \sim 10^{-7} \times L_{\rm Bol}$ up to $10^{-4} \times L_{\rm Bol}$ at high bolometric luminosity. It is often reported that the coupling efficiency predicted by feedback models is significantly higher, for example 5%. On the other hand, only a fraction of the injected energy will become kinetic power in the outflow, while the rest will be used in doing work against the ambient pressure and the gravitational potential for example (see Harrison et al. 2018). From the comparison with the NLR outflows in the SUPER sample, we find that in the majority of cases (12 out of 18) the NLR kinetic power is larger, in five objects they are comparable, and in one case it is the BLR kinetic power that is larger. However, we do not further speculate on such comparisons given the large uncertainties affecting these measurements.

Another fundamental parameter of the outflow is the momentum rate defined as $\dot{P}_{\rm out} = \dot{M}_{\rm out} v^{\rm CIV}_{50}$. In Fig. 16 we plot the outflow momentum load, which is defined as the momentum rate divided by the AGN radiation momentum rate ($\dot{P}_{\rm AGN} = L_{\rm Bol}/c$) as a function of the outflow velocity. The values estimated for the BLR winds of the SUPER sample are very low $\sim[10^{-5} : 10^{-2}]$. For the X-ray winds the theoretical momentum flux is expected to be comparable to $L_{\rm AGN}/c$, that is, a momentum load close to unity (i.e. a momentum conserving outflow). Figure 16 shows the expected momentum load for a momentum-conserving wind model (dashed line). The bulk of the winds in the BLR show lower values than momentum-driven winds (with the larger values being shown by the sources with the larger BLR wind velocities) suggesting that a different form of driving mechanism may be acting at these scales.

6. Conclusions

We present the results of the analysis of 21 Type-1 X-ray-selected AGNs from the SUPER survey (Circosta et al. 2018) with near-infrared SINFONI IFU and UV spectroscopy. The two main goals of the analysis presented in this paper are to (1) derive BH masses and Eddington ratios using virial BH mass estimators based on Hα, Hβ, and MgII; and to 2) trace AGN-driven winds in the BLR using the blueshift of the CIV line profile.

Our main finding can be summarised as follows:

(i) We find that the Hα and Hβ line widths correlate with each other as do the line continuum luminosity at 5100 Å and the Hα line luminosity, resulting in a well-defined correlation between BH mass estimated from Hα and Hβ. The SUPER AGNs exhibit SMBHs with mass in the range Log $(M_{\rm BH}/M_\odot) = 8.5$–$10.8$ and Eddington ratios in the range $0.04 < \lambda < 1.3$.

(ii) We confirm that the CIV line width does not correlate with the Balmer lines and its peak is blueshifted with respect to the [OIII]-based systemic redshift. We interpreted this findings as the presence of outflows in the BLR with derived velocities up to $\sim$4700 km s^{-1}.

(iii) As found previously in Vietri et al. (2018), we confirm the strong correlation between $v^{\rm CIV}_{50}$ and the UV-to-X-ray continuum slope, bolometric luminosity, and Eddington ratio by analysing an unbiased sample of sources. We interpret this in the context of the disc-wind scenario where a high UV luminosity is necessary to launch the wind and softer SEDs can prevent over-ionisation, producing high-velocity BLR winds.

(iv) We compare the properties of the BLR and NLR winds as traced by CIV and [OIII], respectively. We find an anti-correlation between the [OIII] EW and $v^{\rm CIV}_{50}$ and a significant correlation between $v^{\rm [OIII]}_{10}$ and $v^{\rm CIV}_{50}$. From SINFONI IFU data, we know that the gas emitting [OIII] is located at kiloparsec scale distances. We therefore interpret the correlation found as supporting a scenario where BLR winds are capable of affecting the gas in the NLR emission located at kiloparsec distances, likely partially blocking the ionising photons of the NLR or sweeping up the gas in the NLR.

(v) We derive mass outflows rates in the range 0.005–3 $M_\odot$ yr^{-1} for the BLR winds. The mass outflow rate of the

BLR winds shows a correlation with bolometric luminosity as steep as that observed for winds at sub-parsec scale distances and in the NLR. The kinetic power of the BLR winds inferred is $\dot{E}_{\rm kin} \sim 10^{[-7:-4]} \times L_{\rm bol}$, and in 28% of the SUPER sample the kinetic power of the BLR and NLR winds are comparable. Despite the fact that these values are below the coupling efficiency predicted by AGN feedback models, we have to bear in mind that only a fraction of the injected energy will become kinetic power in the outflow.

(vi) The momentum fluxes of the BLR winds normalised by the AGN radiation momentum rate inferred for the SUPER sample are well below theoretical expectations of a momentum-driven wind, indicating that for these winds a different driving mechanism may be acting at these scales.

As discussed in this paper, we are now able, for the first time in an unbiased sample of AGNs at $z \sim 2$, to trace the presence of AGN-driven outflows at $z \sim 2$ over parsec to kiloparsec scales. Moving to even larger scales, the advent of state-of-art IFU facilities such as VLT/MUSE has allowed the elusive material of the circum-galactic medium to be uncovered (e.g. Borisova et al. 2016). Clear evidence of an outflow propagating over dozens of kiloparsec through a metal-enriched circum-galactic medium was recently reported by Travascio et al. (2020) who analysed the VLT/MUSE observations of a WISSH QSO at $z \sim 3.6$, highlighting the importance of using such facilities to map AGN activity over scales of up to tens of kiloparsec in order to study the interplay between nuclear activity and gas content over a very large range in radial distance and trace the impact that the AGN feedback may have on the circum-galactic medium at the peak epoch of cosmic star-formation and AGN activity.

Acknowledgements. We thank the anonymous referee for the useful comments that improved the paper. The scientific results reported in this article are based on observations collected at the European organisation for Astronomical Research in the Southern Hemisphere under ESO programs 196.A-0377 (SINFONI data) and LP175.A-0839 (zCOSMOS data), and SDSS. Funding for SDSS-III has been provided by the Alfred P. Sloan Foundation, the Participating Institutions, the National Science Foundation, and the US Department of Energy Office of Science. The SDSS-III web site is http://www.sdss3.org/. SDSS-III is managed by the Astrophysical Research Consortium for the Participating Institutions of the SDSS-III Collaboration including the University of Arizona, the Brazilian Participation Group, Brookhaven National Laboratory, Carnegie Mellon University, University of Florida, the French Participation Group, the German Participation Group, Harvard University, the Instituto de Astrofisica de Canarias, the Michigan State/Notre Dame/JINA Participation Group, Johns Hopkins University, Lawrence Berkeley National Laboratory, Max Planck Institute for Astrophysics, Max Planck Institute for Extraterrestrial Physics, New Mexico State University, New York University, Ohio State University, Pennsylvania State University, University of Portsmouth, Princeton University, the Spanish Participation Group, University of Tokyo, University of Utah, Vanderbilt University, University of Virginia, University of Washington, and Yale University. This research project was supported by the DFG Cluster of Excellence "Origin and Structure of the Universe" (universe-cluster.de). G. V. acknowledges financial support from Premiale 2015 MITic (PI B. Garilli). G. C., M. Bi, C. F. and F. F. acknowledge support from PRIN MIUR project "Black Hole winds and the Baryon Life Cycle of Galaxies: the stone-guest at the galaxy evolution supper", contract #2017PH3WAT. M. P. is supported by the Programa Atracción de Talento de la Comunidad de Madrid via grant 2018-T2/TIC-11715.

References

Akritas, M. G., & Bershady, M. A. 1996, ApJ, 470, 706
Baron, D., & Netzer, H. 2019, MNRAS, 486, 4290
Baron, D., Stern, J., Poznanski, D., & Netzer, H. 2016, ApJ, 832, 8
Baskin, A., & Laor, A. 2005, MNRAS, 356, 1029
Bentz, M. C., Peterson, B. M., Netzer, H., Pogge, R. W., & Vestergaard, M. 2009, ApJ, 697, 160
Bentz, M. C., Denney, K. D., Grier, C. J., et al. 2013, ApJ, 767, 149
Bischetti, M., Piconcelli, E., Vietri, G., et al. 2017, A&A, 598, A122
Bongiorno, A., Maiolino, R., Brusa, M., et al. 2014, MNRAS, 443, 2077
Borisova, E., Cantalupo, S., Lilly, S. J., et al. 2016, ApJ, 831, 39
Boroson, T. A., & Green, R. F. 1992, ApJS, 80, 109
Bruni, G., Piconcelli, E., Misawa, T., et al. 2019, A&A, 630, A111
Cardelli, J. A., Clayton, G. C., & Mathis, J. S. 1989, ApJ, 345, 245
Carniani, S., Marconi, A., Maiolino, R., et al. 2016, A&A, 591, A28
Circosta, C., Mainieri, V., Padovani, P., et al. 2018, A&A, 620, A82
Civano, F., Marchesi, S., Comastri, A., et al. 2016, ApJ, 819, 62
Coatman, L., Hewett, P. C., Banerji, M., et al. 2017, MNRAS, 465, 2120
Coatman, L., Hewett, P. C., Banerji, M., et al. 2019, MNRAS, 486, 5335
Davies, R. I. 2007, MNRAS, 375, 1099
Denney, K. D. 2012, ApJ, 759, 44
Duras, F., Bongiorno, A., Piconcelli, E., et al. 2017, A&A, 604, A67
Feigelson, E. D., & Nelson, P. I. 1985, ApJ, 293, 192
Ferrarese, L., & Merritt, D. 2000, ApJ, 539, L9
Fiore, F., Feruglio, C., Shankar, F., et al. 2017, A&A, 601, A143
Gaskell, C. M. 1982, ApJ, 263, 79
Gebhardt, K., Bender, R., Bower, G., et al. 2000, ApJ, 539, L13
Georgakakis, A., & Nandra, K. 2011, MNRAS, 414, 992
Graham, A. W., Ciambur, B. C., & Soria, R. 2016, ApJ, 818, 172
Greene, J. E., & Ho, L. C. 2005, ApJ, 630, 122
Harrison, C. M., Costa, T., Tadhunter, C. N., et al. 2018, Nat. Astron., 2, 198
Isobe, T., Feigelson, E. D., & Nelson, P. I. 1986, ApJ, 306, 490
Kakkad, D., Mainieri, V., Vietri, G., et al. 2020, A&A, 642, A147
Kaspi, S., Smith, P. S., Netzer, H., et al. 2000, ApJ, 533, 631
Kaspi, S., Maoz, D., Netzer, H., et al. 2005, ApJ, 629, 61
LaMassa, S. M., Urry, C. M., Cappelluti, N., et al. 2016, ApJ, 817, 172
Lavalley, M., Isobe, T., & Feigelson, E. 1992, in Astronomical Data Analysis Software and Systems I, eds. D. M. Worrall, C. Biemesderfer, & J. Barnes, ASP Conf. Ser., 25, 245
Lira, P., Kaspi, S., Netzer, H., et al. 2018, ApJ, 865, 56
Liu, Z., Merloni, A., Georgakakis, A., et al. 2016, MNRAS, 459, 1602
Magorrian, J., Tremaine, S., Richstone, D., et al. 1998, AJ, 115, 2285
Martocchia, S., Piconcelli, E., Zappacosta, L., et al. 2017, A&A, 608, A51
Marziani, P., Sulentic, J. W., Plauchu-Frayn, I., & del Olmo, A. 2013, A&A, 555, A89
Marziani, P., Martínez Carballo, M. A., Sulentic, J. W., et al. 2016, Ap&SS, 361, 29
Matsuoka, K., Nagao, T., Marconi, A., Maiolino, R., & Taniguchi, Y. 2011, A&A, 527, A100
McGill, K. L., Woo, J.-H., Treu, T., & Malkan, M. A. 2008, ApJ, 673, 703
McLure, R. J., & Jarvis, M. J. 2002, MNRAS, 337, 109
Mejía-Restrepo, J. E., Trakhtenbrot, B., Lira, P., Netzer, H., & Capellupo, D. M. 2016, MNRAS, 460, 187
Mejía-Restrepo, J. E., Lira, P., Netzer, H., Trakhtenbrot, B., & Capellupo, D. M. 2018, Nat. Astron., 2, 63
Menzel, M. L., Merloni, A., Georgakakis, A., et al. 2016, MNRAS, 457, 110
Nagao, T., Marconi, A., & Maiolino, R. 2006, A&A, 447, 157
Netzer, H. 2013, The Physics and Evolution of Active Galactic Nuclei (UK: Cambridge University Press)
Netzer, H. 2020, MNRAS, 494, 1611
Osterbrock, D. E., & Ferland, G. J. 2006, Astrophysics of Gaseous Nebulae and Active Galactic Nuclei (Sausalito, CA: University Science Books)
Popović, L., Kovačević-Dojčinović, J., & Marčeta-Mandić, S. 2019, MNRAS, 484, 3180
Richards, G. T., Kruczek, N. E., Gallagher, S. C., et al. 2011, AJ, 141, 167
Runnoe, J. C., Brotherton, M. S., & Shang, Z. 2012, MNRAS, 427, 1800
Schwarz, G. 1978, Ann. Stat., 6, 461
Shen, Y. 2013, Bull. Astron. Soc. India, 41, 61
Shen, Y., & Liu, X. 2012, ApJ, 753, 125
Shen, Y., Greene, J. E., Strauss, M. A., Richards, G. T., & Schneider, D. P. 2008, ApJ, 680, 169
Shen, Y., Richards, G. T., Strauss, M. A., et al. 2011, ApJS, 194, 45
Suh, H., Hasinger, G., Steinhardt, C., Silverman, J. D., & Schramm, M. 2015, ApJ, 815, 129
Suh, H., Civano, F., Trakhtenbrot, B., et al. 2020, ApJ, 889, 32
Sulentic, J. W., Marziani, P., & Dultzin-Hacyan, D. 2000, ARA&A, 38, 521
Sulentic, J. W., Bachev, R., Marziani, P., Negrete, C. A., & Dultzin, D. 2007, ApJ, 666, 757
Trakhtenbrot, B., & Netzer, H. 2012, MNRAS, 427, 3081
Travascio, A., Zappacosta, L., Cantalupo, S., et al. 2020, A&A, 635, A157
Tsuzuki, Y., Kawara, K., Yoshii, Y., et al. 2006, ApJ, 650, 57
Véron-Cetty, M.-P., Joly, M., & Véron, P. 2004, A&A, 417, 515
Vestergaard, M. 2002, ApJ, 571, 733
Vietri, G., Piconcelli, E., Bischetti, M., et al. 2018, A&A, 617, A81
Wang, J.-G., Dong, X.-B., Wang, T.-G., et al. 2009, ApJ, 707, 1334
Woo, J.-H., Yoon, Y., Park, S., Park, D., & Kim, S. C. 2015, ApJ, 801, 38
Wu, X. B., Wang, R., Kong, M. Z., Liu, F. K., & Han, J. L. 2004, A&A, 424, 793
Zappacosta, L., Piconcelli, E., Giustini, M., et al. 2020, A&A, 635, L5

[1] INAF – Istituto di Astrofisica Spaziale e Fisica Cosmica Milano, Via Alfonso Corti 12, 20133 Milano, Italy
e-mail: giustina.vietri@inaf.it
[2] Cluster of Excellence, Boltzmann-Str. 2, 85748 Garching bei München, Germany
[3] European Southern Observatory, Karl-Schwarzschild-Strasse 2, Garching bei München, Germany
[4] European Southern Observatory, Alonso de Cordova 3107, Vitacura, Casilla 19001, Santiago de Chile, Chile
[5] School of Physics and Astronomy, Tel-Aviv University, Tel-Aviv 69978, Israel
[6] Centro de Astrobiología (CAB, CSIC–INTA), Departamento de Astrofísica, Cra. de Ajalvir Km. 4, 28850 Torrejón de Ardoz, Madrid, Spain
[7] INAF – Osservatorio Astrofisico di Arcetri, Largo E. Fermi 5, 50125 Firenze, Italy
[8] Department of Physics & Astronomy, University College London, Gower Street, London WC1E 6BT, UK
[9] School of Mathematics, Statistics and Physics, Newcastle University, Newcastle upon Tyne NE1 7RU, UK
[10] INAF – Osservatorio Astronomico di Roma, Via Frascati 33, 00078 Monte Porzio Catone, Roma, Italy
[11] Max-Planck-Institut für Astronomie, Königstuhl 17, 69117 Heidelberg, Germany
[12] INAF – Osservatorio Astronomico di Trieste, via G.B. Tiepolo 11, 34143 Trieste, Italy
[13] Dipartimento di Fisica e Astronomia dell'Universitá degli Studi di Bologna, via P. Gobetti 93/2, 40129 Bologna, Italy
[14] INAF/OAS, Osservatorio di Astrofisica e Scienza dello Spazio di Bologna, via P. Gobetti 93/3, Bologna, Italy
[15] Scuola Normale Superiore, Piazza dei Cavalieri 7, 56126 Pisa, Italy
[16] Institute of Theoretical Astrophysics, University of Oslo, PO Box 1029, Blindern, 0315 Oslo, Norway
[17] Dipartimento di Fisica e Astronomia, Universitá di Firenze, Via G. Sansone 1, 50019 Firenze, Sesto Fiorentino, Italy
[18] CEA, IRFU, DAp, AIM, Université Paris-Saclay, Université Paris Diderot, Sorbonne Paris Cité, CNRS, 91191 Gif-sur-Yvette 9, France
[19] INAF – Osservatorio Astronomico di Padova, Vicolo dell'Osservatorio 5, 35122 Padova, Italy
[20] Centre for Extragalactic Astronomy, Department of Physics, Durham University, South Road, Durham DH1 3LE, UK
[21] Max-Planck-Institut für extraterrestrische Physik (MPE), Giessenbachstrasse 1, 85748 Garching bei München, Germany
[22] Graduate school of Science and Engineering, Saitama Univ. 255 Shimo-Okubo, Sakura-ku, Saitama City, Saitama 338-8570, Japan
[23] National Astronomical Observatory of Japan, Mitaka 181-8588, Tokyo, Japan
[24] Chalmers University of Technology, Department of Earth and Space Sciences, Onsala Space Observatory, 43992 Onsala, Sweden

Appendix A: Integrated spectra of Type-1 SUPER sample

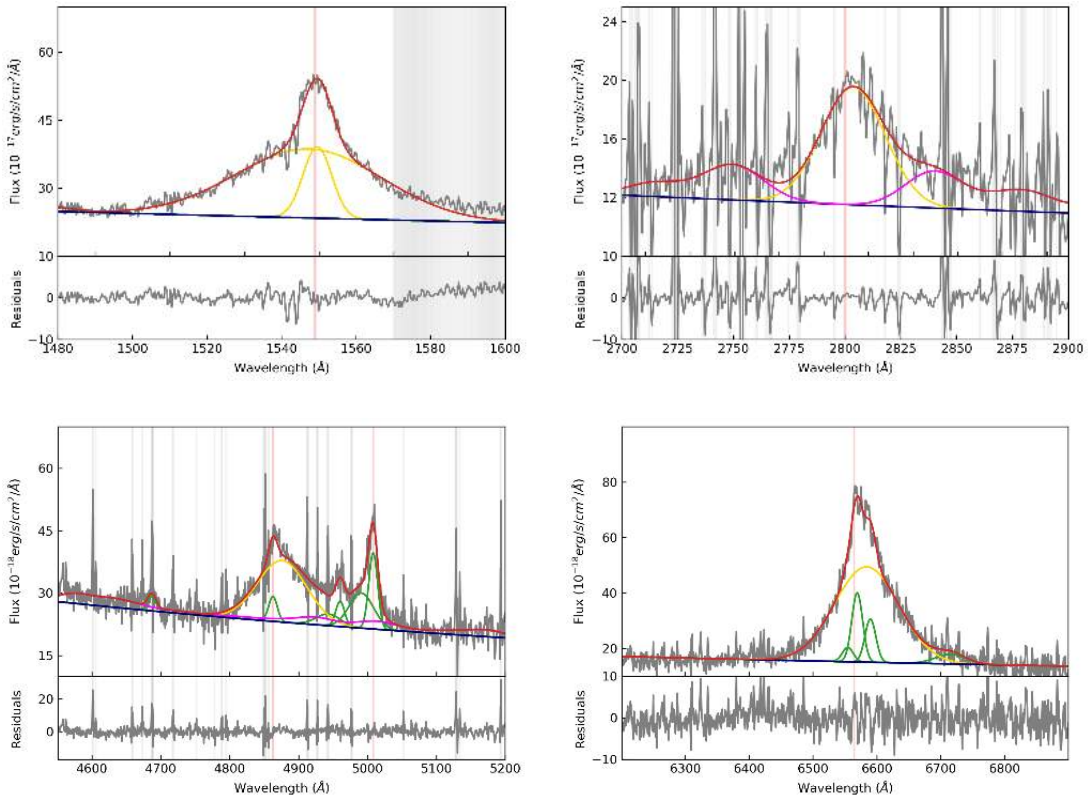

Fig. A.1. Integrated spectra from the CIV-MgII region (*upper panels*) to Hβ-Hα region (*lower panels*) of the SUPER targets X_N_160_22. The grey curve shows the observed spectrum, the red curve shows the reproduced overall emission line model, the magenta curve shows the iron emission, the blue navy curves show the continuum model, and the green curves show the individual Gaussian components used to reproduce the profiles of all the emission lines. The BLR component is shown as a gold Gaussian profile. The red vertical lines indicate the location of each line at systemic velocity. The vertical grey regions mark the channels with strong skylines which were masked during the fitting procedure. The *x*- and *y*-axis show the rest frame wavelength and flux (not corrected for extinction) according to the redshift of each target.

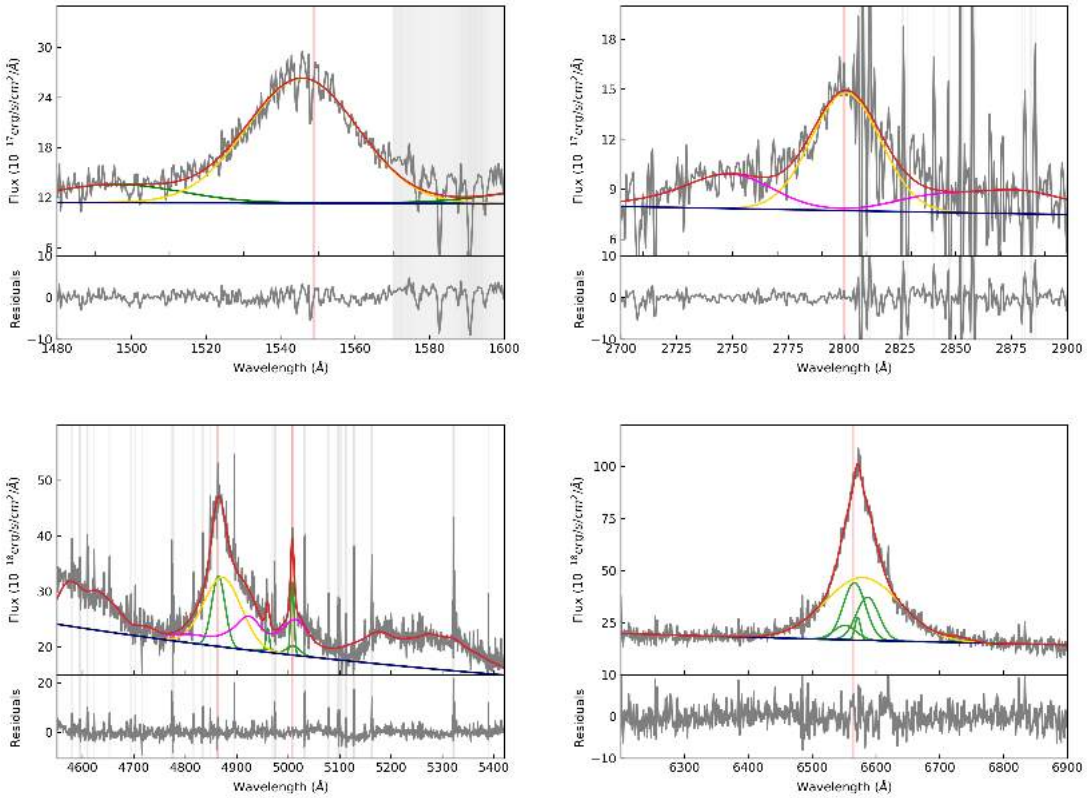

Fig. A.2. X_N_81_44. The modelling is the same as in Fig. A.1.

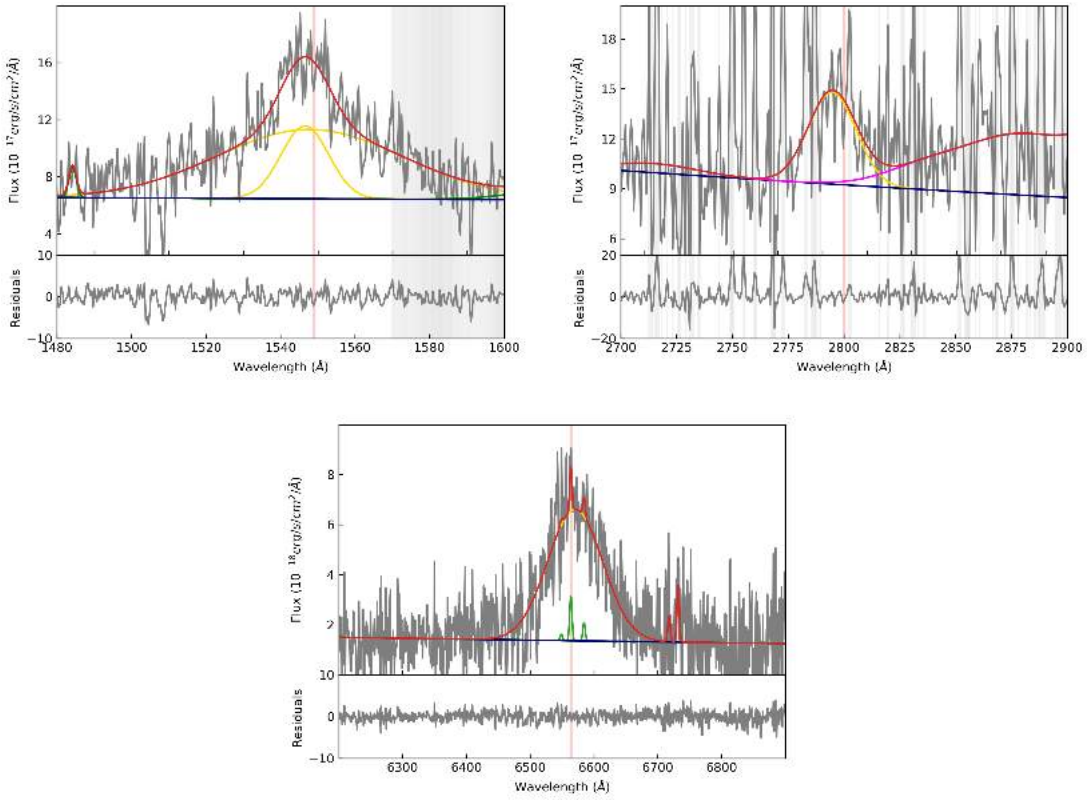

Fig. A.3. X_N_53_3. The modelling is the same as in Fig. A.1.

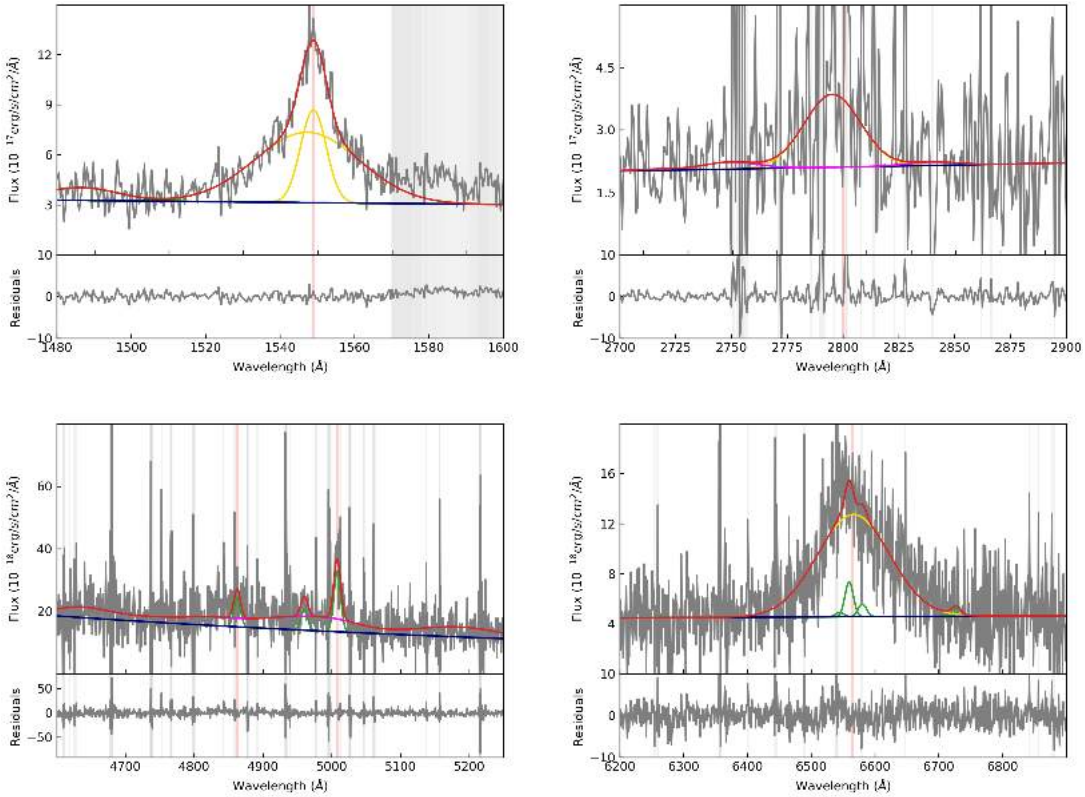

Fig. A.4. X_N_66_23. The modelling is the same as in Fig. A.1.

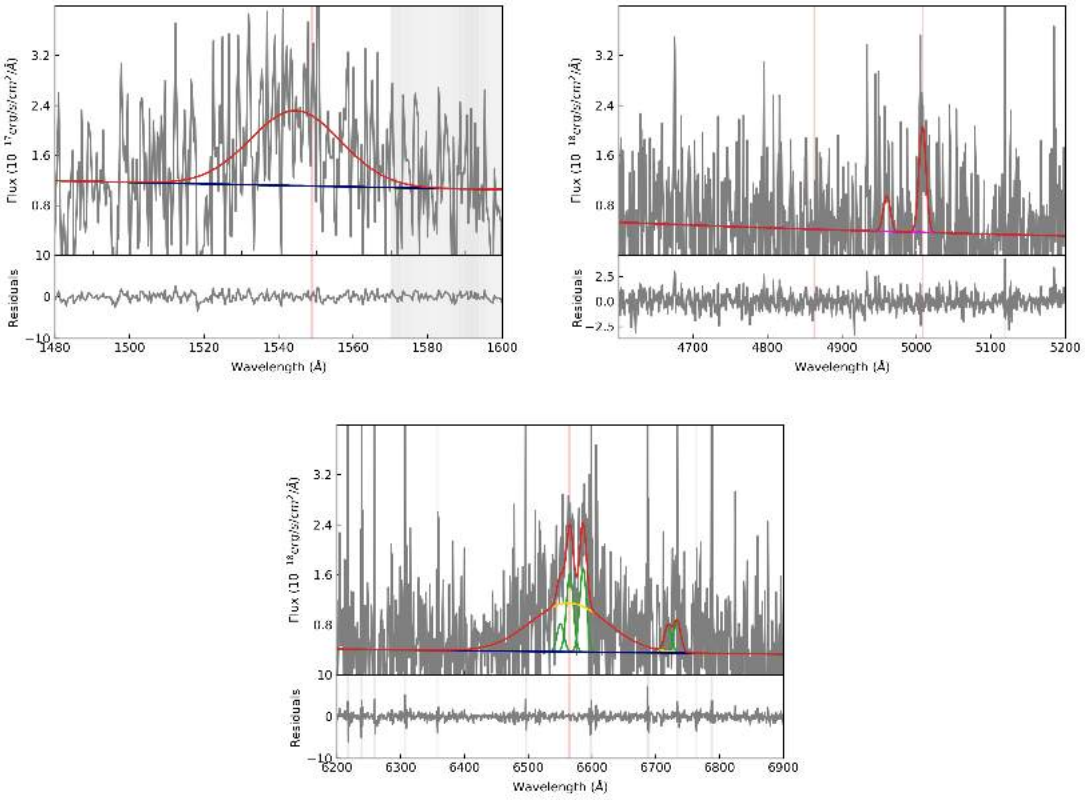

Fig. A.5. X_N_35_20. The modelling is the same as in Fig. A.1.

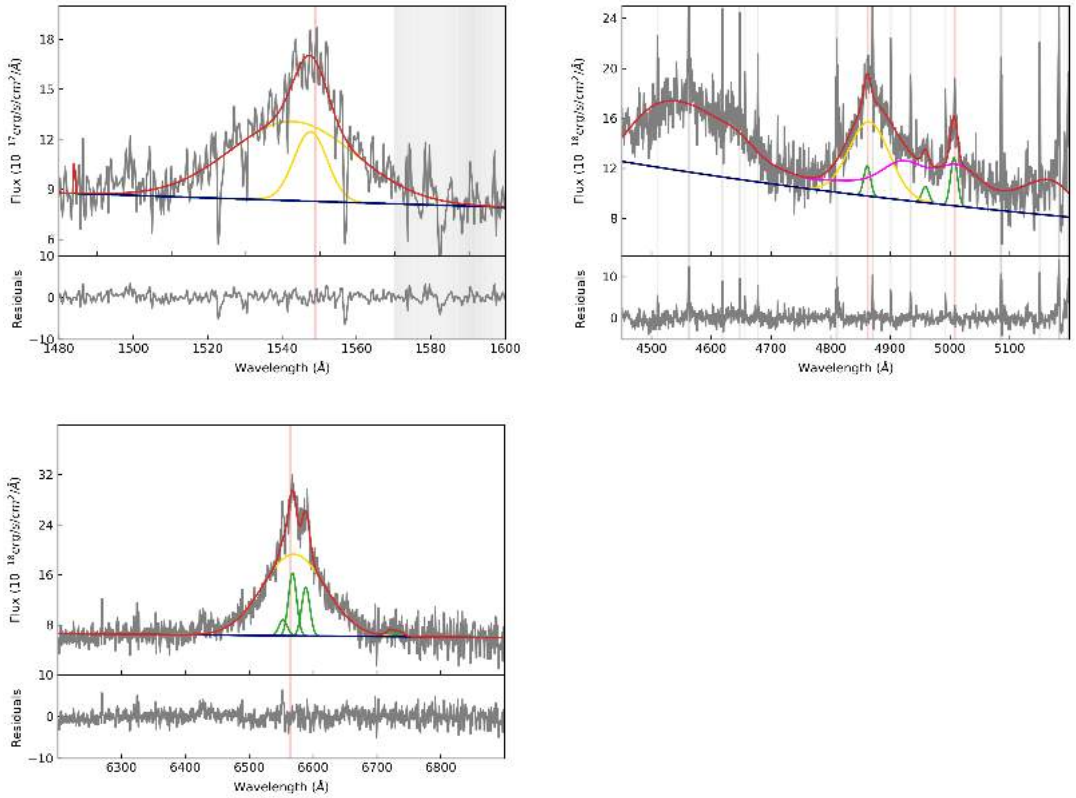

Fig. A.6. X_N_12_26. The modelling is the same as in Fig. A.1.

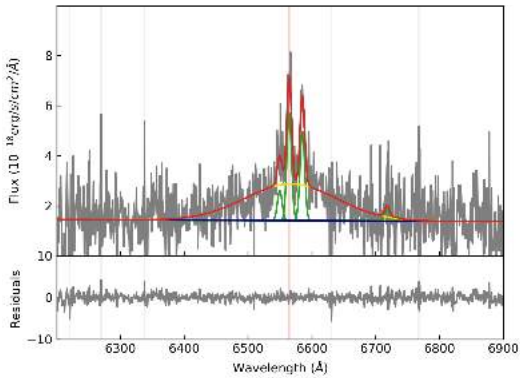

Fig. A.7. X_N_44_64. The modelling is the same as in Fig. A.1.

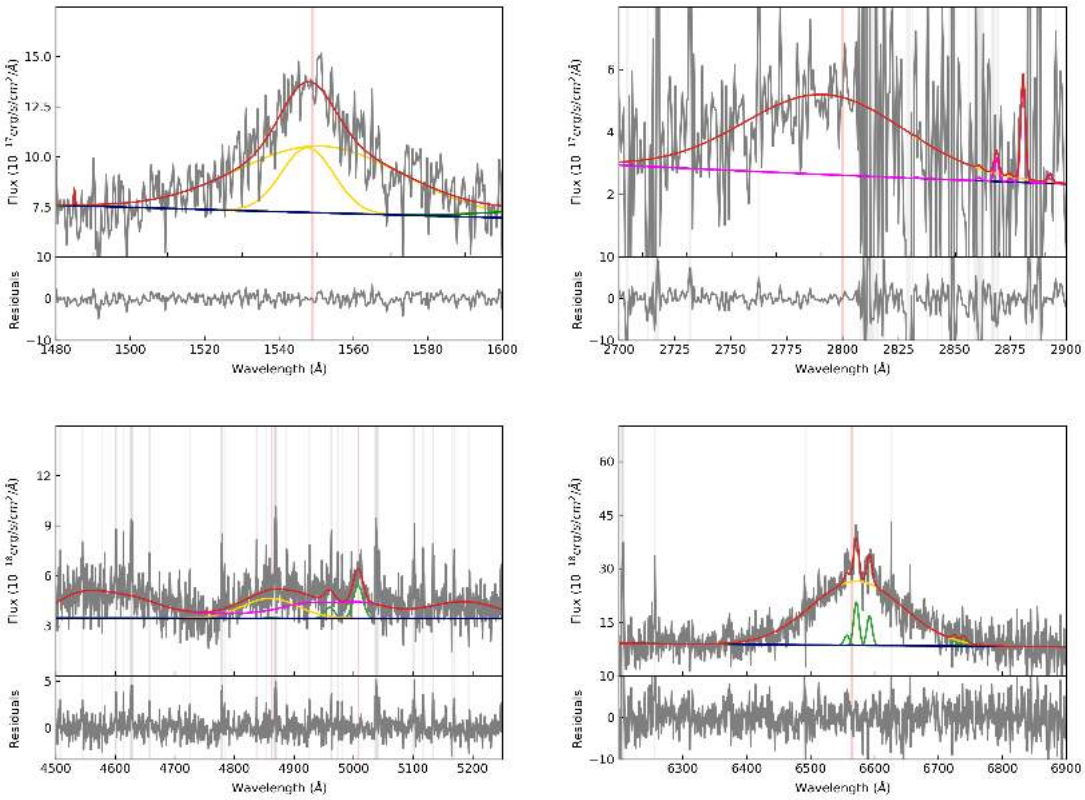

Fig. A.8. X_N_4_48. The modelling is the same as in Fig. A.1.

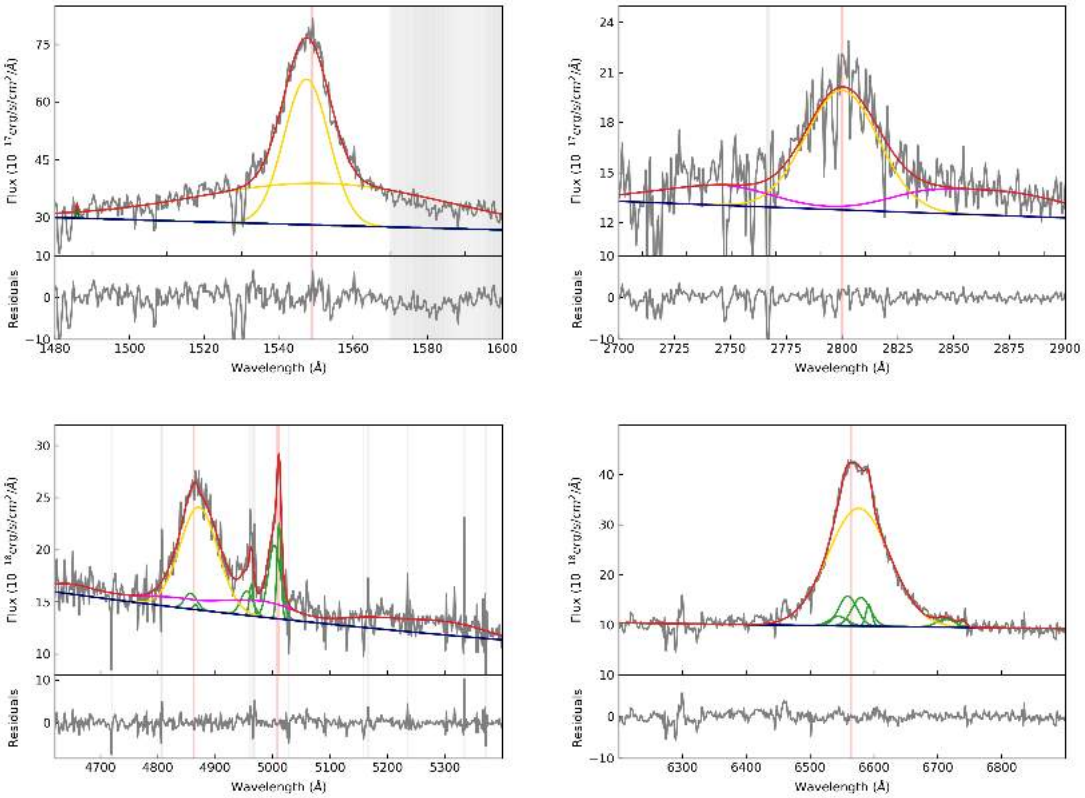

Fig. A.9. X_N_102_35. The modelling is the same as in Fig. A.1.

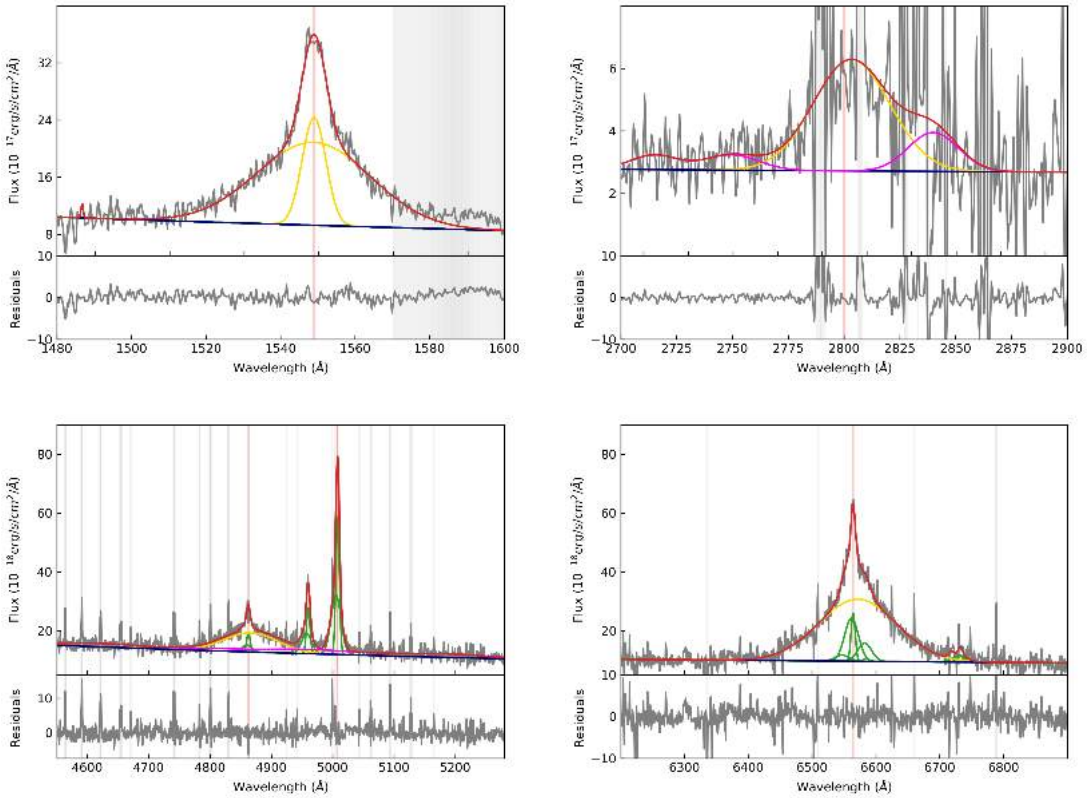

Fig. A.10. X_N_115_23. The modelling is the same as in Fig. A.1.

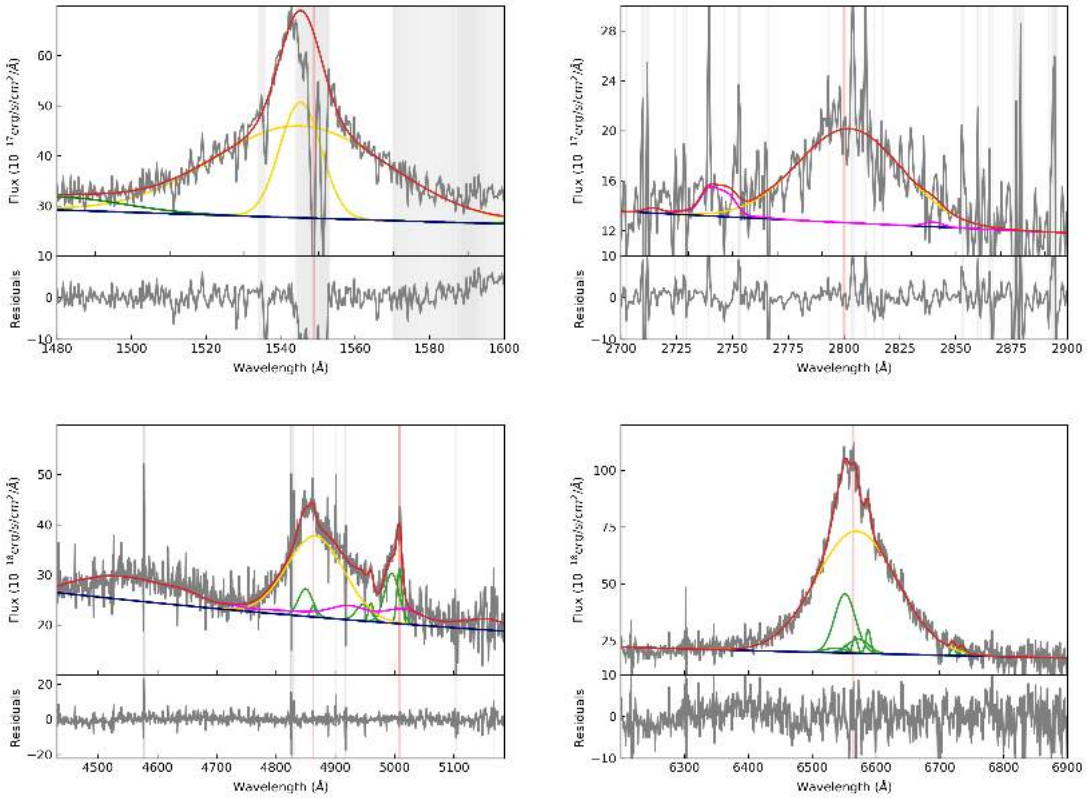

Fig. A.11. cid_166. The modelling is the same as in Fig. A.1.

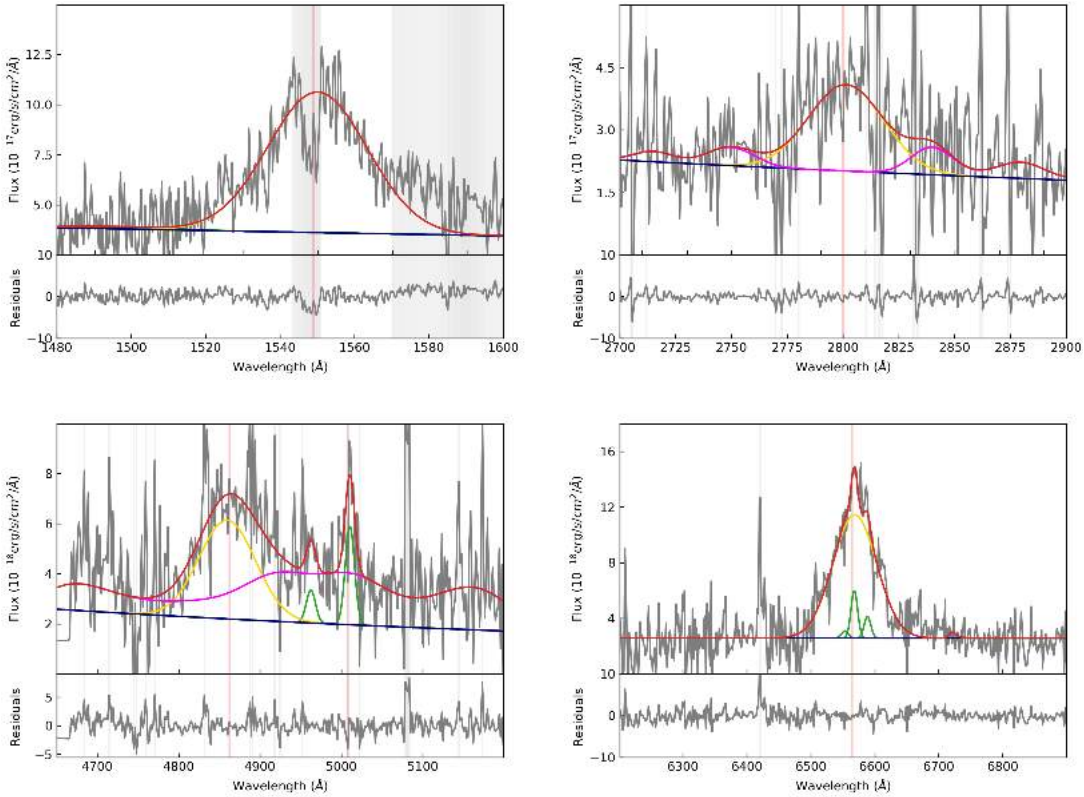

Fig. A.12. cid_1605. The modelling is the same as in Fig. A.1.

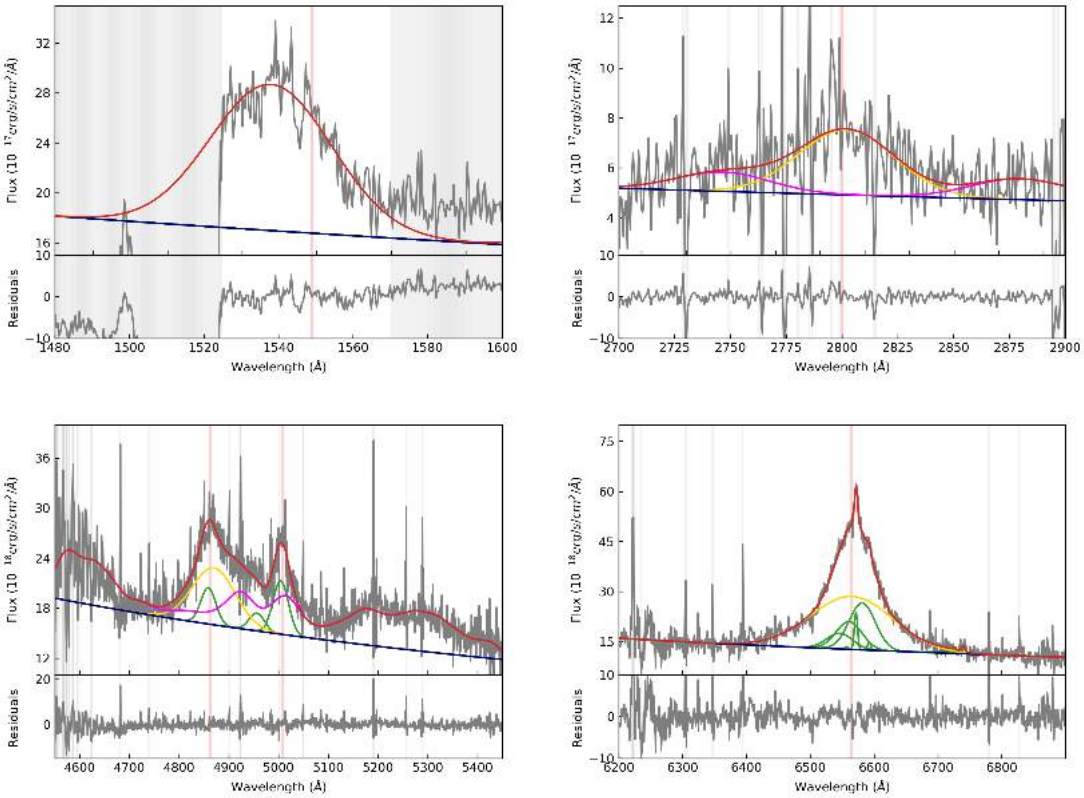

Fig. A.13. cid_346. The modelling is the same as in Fig. A.1.

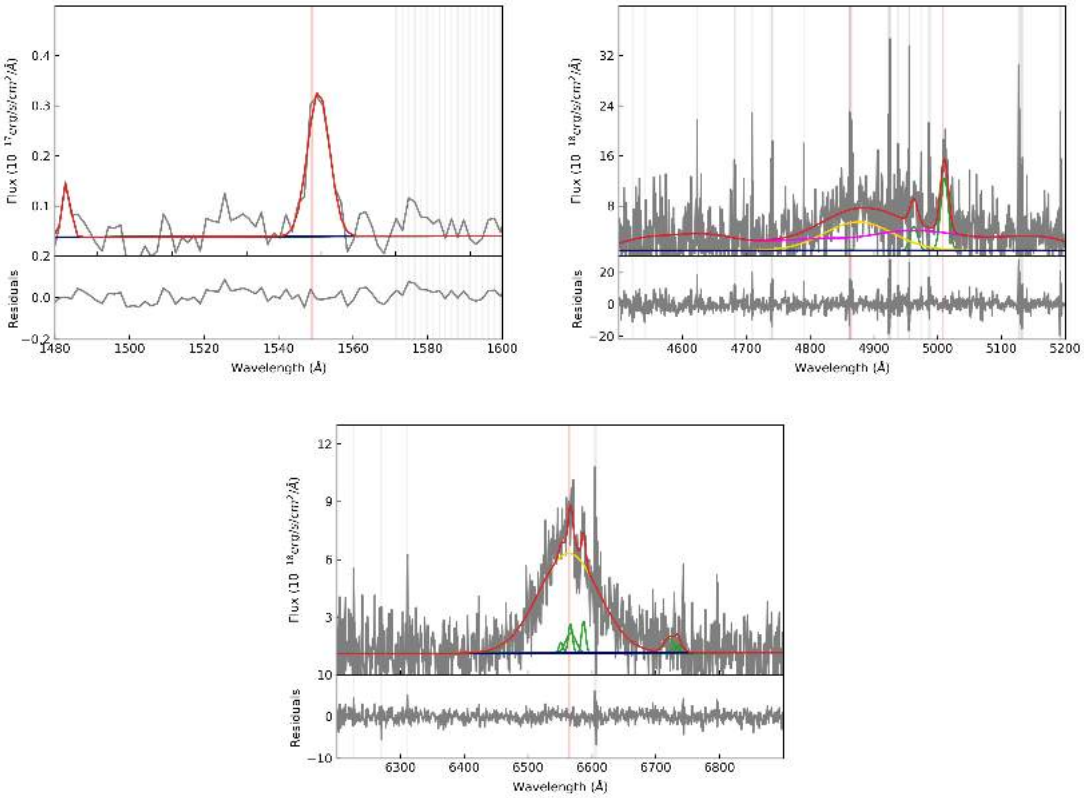

Fig. A.14. cid_1205. The modelling is the same as in Fig. A.1.

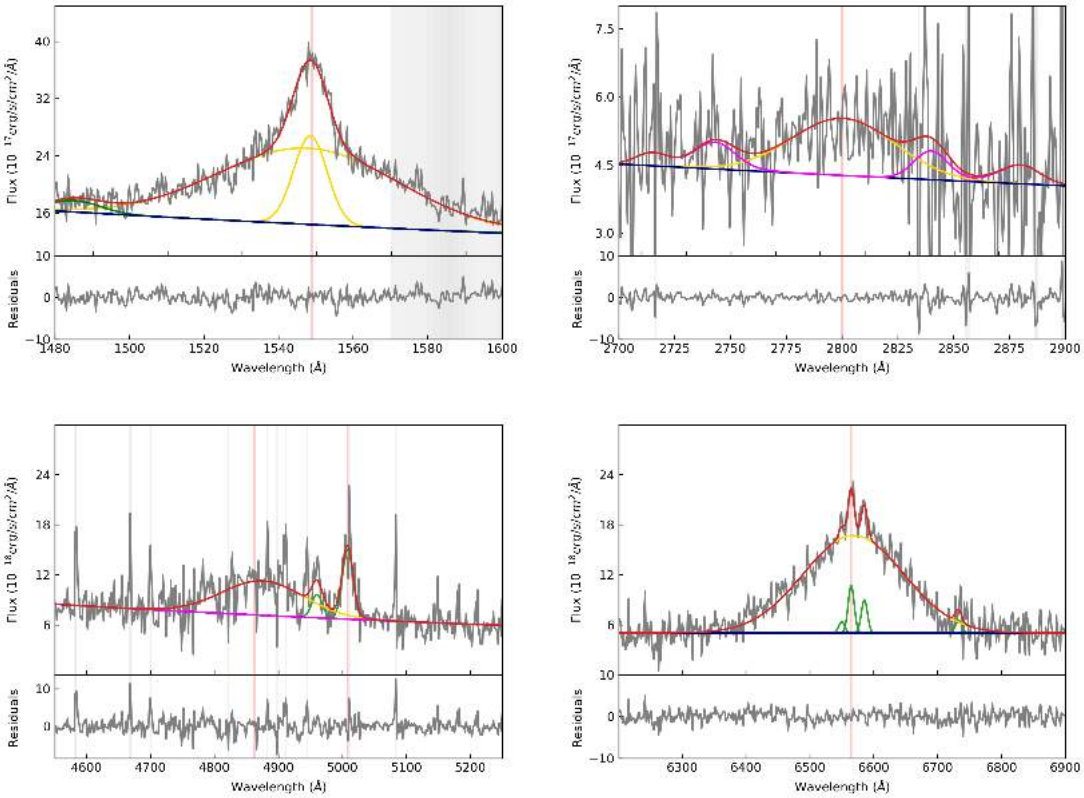

Fig. A.15. cid_467. The modelling is the same as in Fig. A.1.

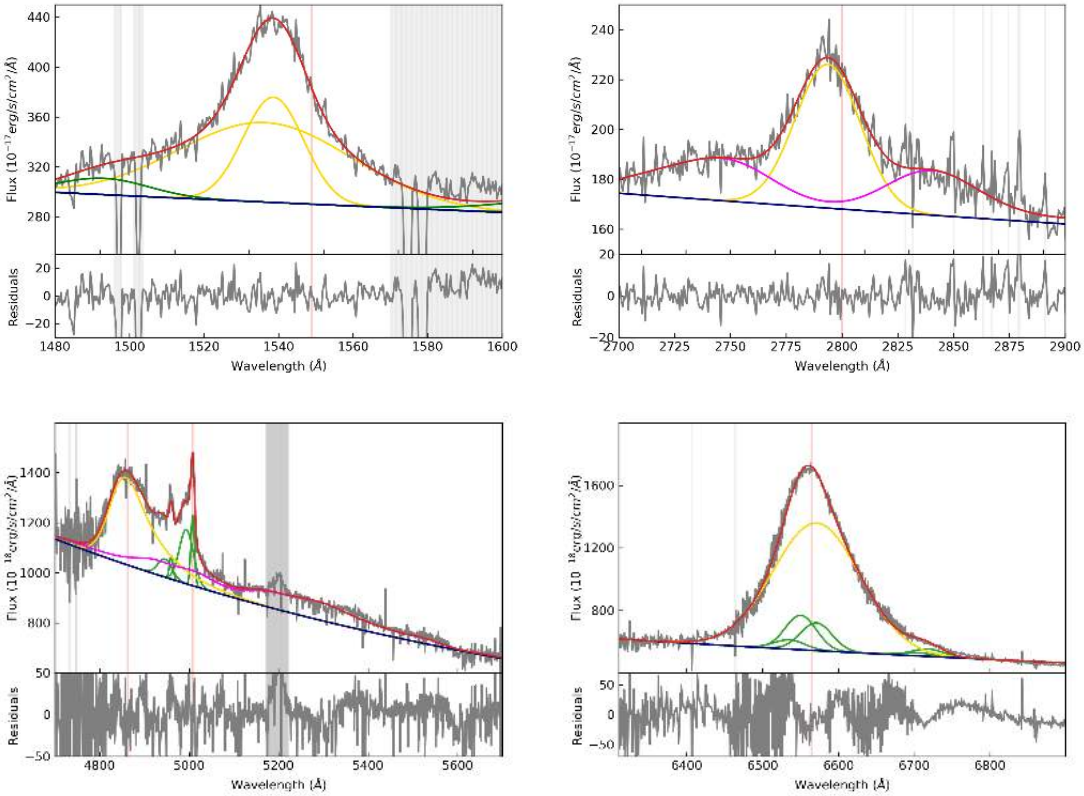

Fig. A.16. J1333+1649. The modelling is the same as in Fig. A.1.

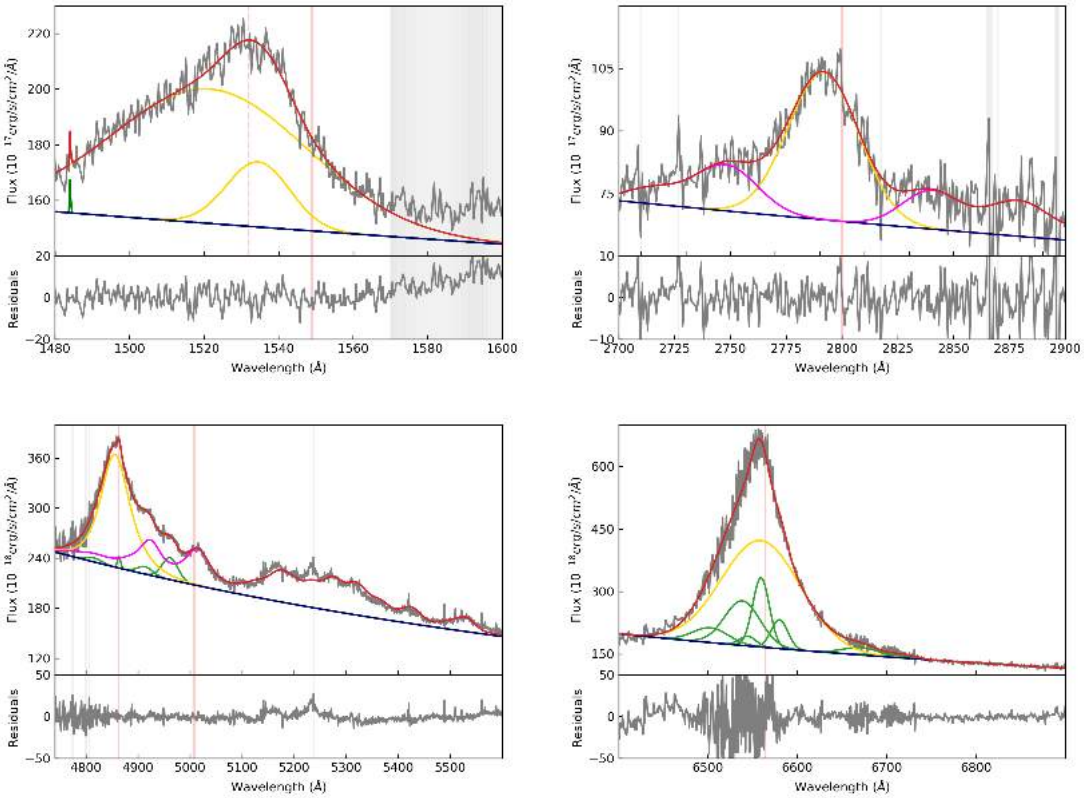

Fig. A.17. J1441+0454. The modelling is the same as in Fig. A.1.

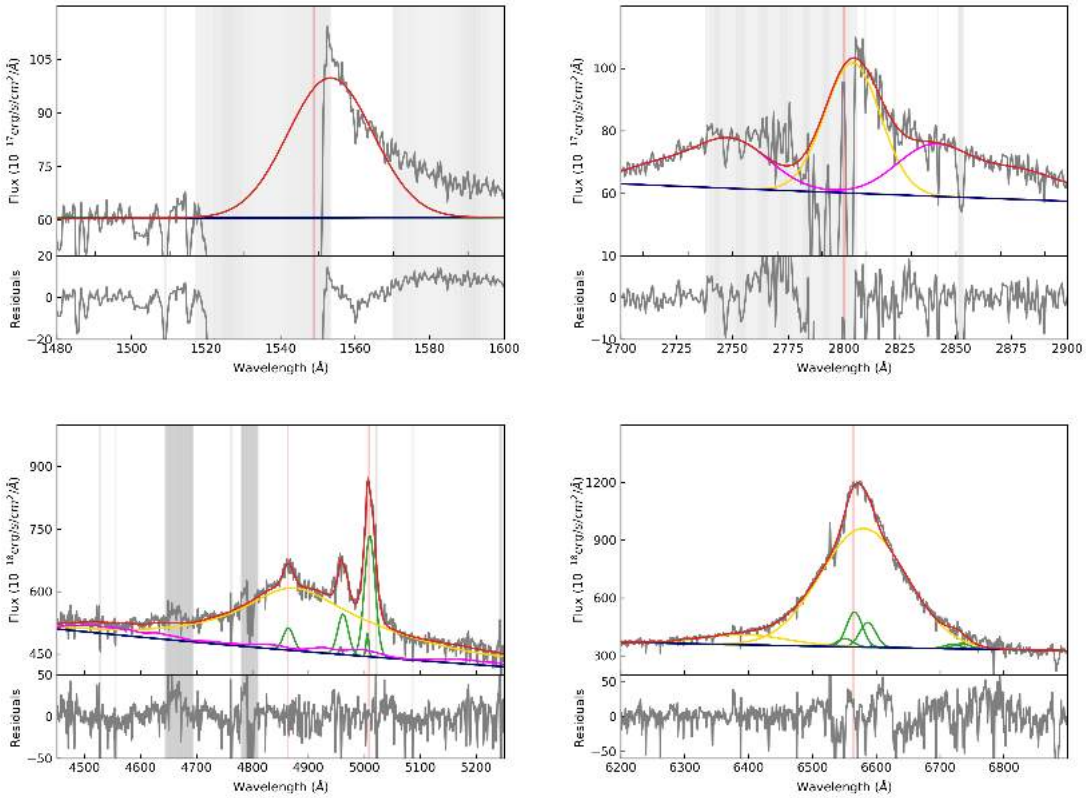

Fig. A.18. J1549+1245. The modelling is the same as in Fig. A.1. We added one Gaussian component around 6380 Å to reduce the χ^2 of our fit (e.g. Carniani et al. 2016).

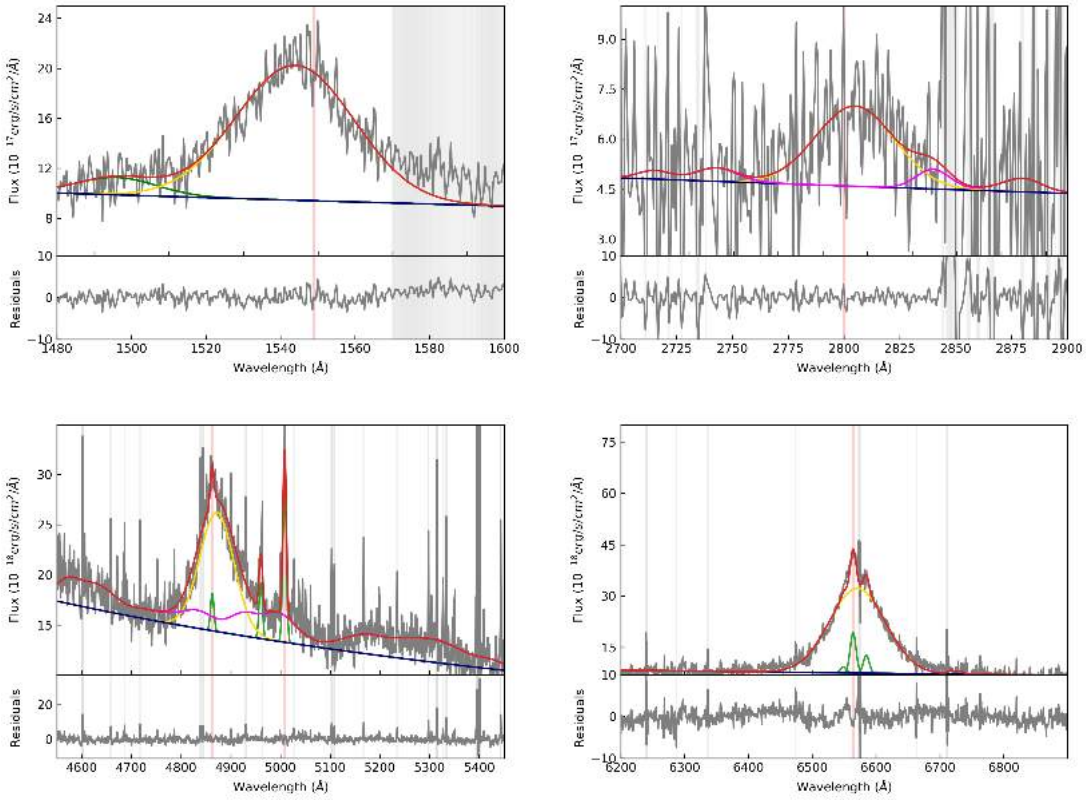

Fig. A.19. S82X1905. The modelling is the same as in Fig. A.1.

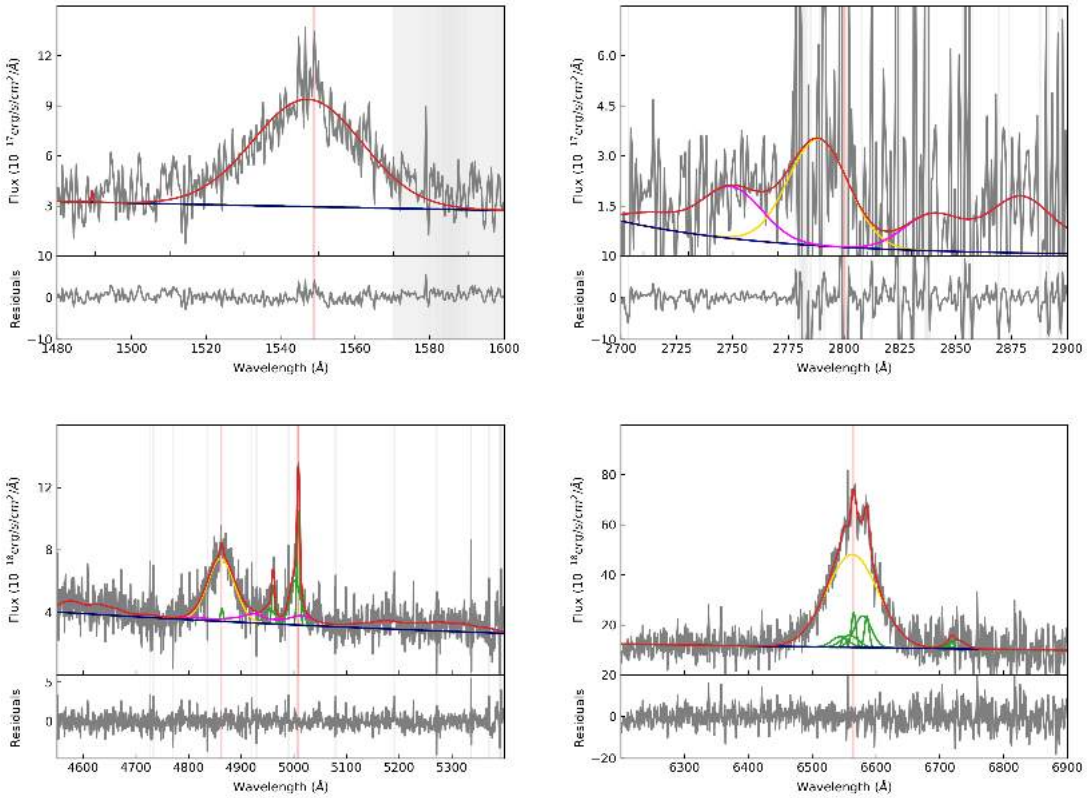

Fig. A.20. S82X1940. The modelling is the same as in Fig. A.1.

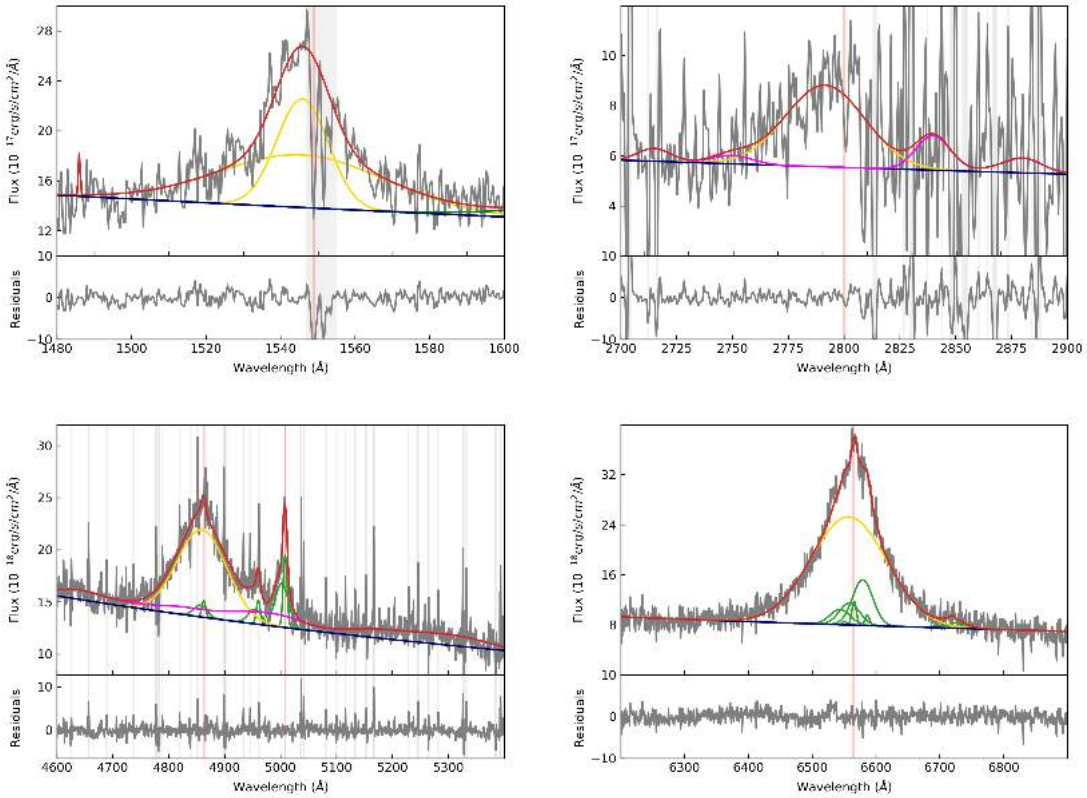

Fig. A.21. S82X2058. The modelling is the same as in Fig. A.1.